

The first galaxies: simulating their feedback-regulated assembly

Myoungwon Jeon^{1*}, Volker Bromm¹, Andreas H. Pawlik² and Miloš Milosavljević¹

¹*Department of Astronomy, University of Texas, Austin, TX 78712, USA*

²*Max-Planck-Institut für Astrophysik, Karl-Schwarzschild-Strasse 1, 85748 Garching bei München, Germany*

ABSTRACT

We investigate the formation of a galaxy reaching a virial mass of $\approx 10^8 M_\odot$ at $z \approx 10$ by carrying out a zoomed radiation-hydrodynamical cosmological simulation. This simulation traces Population III (Pop III) star formation, characterized by a modestly top-heavy initial mass function (IMF), and considers stellar feedback such as photoionization heating from Pop III and Population II (Pop II) stars, mechanical and chemical feedback from supernovae (SNe), and X-ray feedback from accreting black holes (BHs) and high-mass X-ray binaries (HMXBs). We self-consistently impose a transition in star formation mode from top-heavy Pop III to low-mass Pop II, and find that the star formation rate in the computational box is dominated by Pop III until $z \sim 13$, and by Pop II thereafter. The simulated galaxy experiences bursty star formation, with a substantially reduced gas content due to photoionization heating from Pop III and Pop II stars, together with SN feedback. All the gas within the simulated galaxy is metal-enriched above $10^{-5} Z_\odot$, such that there are no remaining pockets of primordial gas. The simulated galaxy has an estimated observed flux of $\sim 10^{-3}$ nJy, which is too low to be detected by the James Webb Space Telescope (JWST) without strong lensing amplification. We also show that our simulated galaxy is similar in terms of stellar mass to Segue 2, the least luminous dwarf known in the Local Group.

Key words: cosmology: theory – galaxies: formation – galaxies: high-redshift – HII regions – hydrodynamics – intergalactic medium – supernovae: physics.

1 INTRODUCTION

An important goal of modern cosmology is to understand the formation and properties of early galaxies that formed a few hundred million years after the Big Bang (Bromm & Yoshida 2011; Loeb & Furlanetto 2013; Wiklind et al. 2013). In the context of hierarchical cosmology, where small structures form first and evolve into bigger systems, dwarf galaxies with virial masses of $M_{\text{vir}} = 10^7 - 10^9 M_\odot$ at $z \simeq 6-15$ were the basic building blocks of large galaxies seen today. Furthermore, it is thought that these galaxies played a pivotal role in reionizing the Universe, the global phase transition from an early neutral medium to a fully ionized one (for reviews see, e.g. Barkana & Loeb 2007; Furlanetto et al. 2006; Robertson et al. 2010). Specifically, the first galaxies were the drivers of the initial stages of reionization (Haardt & Madau 2012; Shull et al. 2012; Robertson et al. 2013).

Over the past decade, there have been enormous efforts to push the high redshift frontier to $z \simeq 7$, detecting light from galaxies with a stellar mass of $M_* \gtrsim 10^8 M_\odot$ (e.g. Bouwens et al. 2011; Oesch et al. 2012; Finkelstein 2013; Schenker et al. 2014; Stark et al. 2015). To assess the observability of even smaller galaxies, and galaxies at even higher redshifts, we need to predict the prop-

erties of the first galaxies by pushing numerical simulations to new levels of physical realism and detail. Our goal here is to derive ab-initio predictions for key quantities, such as their stellar population mix, quantified by a possibly time-variable initial mass function (IMF), star formation rates (SFRs), metallicities, and resulting broad-band colour and recombination-line spectra (e.g. Johnson et al. 2009; Pawlik et al. 2011; Zackrisson et al. 2011). A SFR above $0.1 M_\odot \text{ yr}^{-1}$, corresponding to $M_* \sim 10^7 M_\odot$, might be required for galaxies at $z \gtrsim 10$ to be observed with the *James Webb Space Telescope (JWST)* (e.g. Inoue 2011; Pawlik et al. 2013). For *JWST* deep fields to reach even fainter systems, a magnification boost from gravitational lensing may be required (Zackrisson et al. 2012, 2015).

The properties of such early galaxies were determined by the feedback from preceding generations of stars (for a review see, e.g. Ciardi & Ferrara 2005). The first generation of stars, the so-called Population III (Pop III), formed at $z \lesssim 30$ in dark matter (DM) minihaloes with $M_{\text{vir}} = 10^5 - 10^6 M_\odot$, predominately via ro-vibrationally excited molecular hydrogen (H_2) cooling (e.g. Haiman et al. 1996; Tegmark et al. 1997; Bromm et al. 2002; Yoshida et al. 2003). Radiation from Pop III stars dramatically altered the gas within their host minihaloes, through photoionization, photoheating, and photoevaporation (e.g. Kitayama et al. 2004; Whalen et al. 2004; Alvarez et al. 2006; Yoshida et al. 2007; Wise

* E-mail: myjeon@astro.as.utexas.edu

& Abel 2008). Once a Pop III star died as a supernova (SN), heavy elements were dispersed, enriching the intra-host and intergalactic medium (IGM), thus initiating the prolonged process of chemical evolution (reviewed in Karlsson et al. 2013). The resulting SN feedback from the first stars greatly affected the gas in the shallow potential wells of the host systems (e.g. Greif et al. 2007, 2010; Whalen et al. 2008). The more distant, diffuse IGM was heated as well by X-rays emitted by accreting single black holes (BHs), or high-mass X-ray binaries (HMXBs), both remnants of Pop III stars (e.g. Glover & Brand 2003; Kuhlen & Madau 2005; Milosavljević et al. 2009a,b; Alvarez et al. 2009; Mirabel et al. 2011; Wheeler & Johnson 2011; Hummel et al. 2014; Jeon et al. 2012, 2014a; Xu et al. 2014).

The critical role of feedback from stars in massive galaxies with $M_{\text{vir}} \sim 10^9 - 10^{13} M_{\odot}$ is also emphasized by many authors (e.g. Schaye et al. 2010; Stinson et al. 2013; Kim et al. 2013; Wise et al. 2014). Photoionization, radiation pressure, and SN feedback operate in a non-linear, coupled fashion, such that considering a full treatment of the radiation-hydrodynamics and time dependence of these feedback mechanisms is necessary to reproduce the observed histories of star formation, including their stochastic nature, particularly in dwarf galaxies (e.g. Pawlik et al. 2009; Hopkins et al. 2014). However, due to the prohibitive computational cost related to the baryonic physics, simulating the assembly of massive galaxies from first principles is not feasible. The first dwarf galaxies with virial masses $M_{\text{vir}} \lesssim 10^9$, where such ab-initio modeling is coming within reach, thus provide us with ideal laboratories to develop a detailed theory of feedback-regulated galaxy formation.

The birth of the first galaxies is often defined by theorists as the emergence of atomic cooling haloes, systems assembled at $z \lesssim 15$ with masses of $M_{\text{vir}} \gtrsim 5 \times 10^7 M_{\odot}$, within which the primordial gas was able to cool via atomic hydrogen lines instead of molecular hydrogen (e.g. Oh & Haiman 2002; Bromm & Loeb 2003a). The deeper potential wells of these haloes allowed them to sustain self-regulated star formation in a multi-phase medium by holding on to the gas driven out by stellar feedback. Another feature that renders the atomic cooling haloes viable first galaxy candidates is the presence of supersonic turbulence, which is believed to play an important role in present-day star formation (McKee & Ostriker 2007). Such turbulence is expected to develop during the build-up of the first galaxies due to the inflow of cold gas along cosmic filaments (e.g. Wise & Abel 2007; Greif et al. 2008; Safranek-Shrader et al. 2012).

The relative importance of Pop III stellar feedback on first galaxy formation is determined by the mass range of Pop III stars (e.g. Bromm 2013). Stars with initial masses in the range of $40 M_{\odot} - 140 M_{\odot}$, or larger than $260 M_{\odot}$, are expected to directly collapse into BHs, whereas they undergo pair-instability supernovae (PISNe) in the range of $140 M_{\odot} - 260 M_{\odot}$ (Heger & Woosley 2002). The PISN range can be extended down to $\sim 85 M_{\odot}$ if the progenitor is rapidly rotating (Chatzopoulos & Wheeler 2012; Yoon et al. 2012). Finally, stars with masses between $8 M_{\odot}$ and $40 M_{\odot}$ likely died as conventional core-collapse SNe (CCSNe), or energetic hypernovae in case of high rotation rates (e.g. Umeda & Nomoto 2005).

Earlier studies had predicted that the first stars formed in isolation, with a characteristic mass of $\sim 100 M_{\odot}$ (e.g. Abel et al. 2002; Bromm et al. 2002; Yoshida et al. 2006). However, recent high-resolution simulations, exploring the high densities encountered in protostellar disks, have suggested that the primordial cloud can further fragment, giving rise to the possibility of binary or multiple systems (Turk et al. 2009; Stacy et al. 2010; Clark et al. 2011;

Prieto et al. 2011; Smith et al. 2011; Greif et al. 2011, 2012; Stacy et al. 2012; Dopcke et al. 2013). Radiation-hydrodynamical simulations that take into account the feedback from the protostellar radiation suggest that the first stars typically reached masses of a few $\sim 10 M_{\odot}$ (e.g. Hosokawa et al. 2011; Stacy et al. 2012; Hirano et al. 2014; Susa et al. 2014). If this is indeed the case, the feedback from primordial stars would have been less disruptive than previously thought (Kitayama & Yoshida 2005; Whalen et al. 2008; Chiaki et al. 2013). Specifically, PISN events would have been less frequent, with the majority of Pop III stars now expected to die as CCSNe. It is therefore important to revisit the assembly process of the first galaxies, taking this change in characteristic Pop III mass scale into account.

Most previous studies have been focusing on the feedback from massive Pop III stars ($\gtrsim 100 M_{\odot}$) on first galaxy formation (e.g. Wise & Abel 2008; Greif et al. 2010; Wise et al. 2012; Pawlik et al. 2013; Muratov et al. 2013; Xu et al. 2013; Wise et al. 2014). One prominent result is that even a single PISN with an explosion energy of $E_{\text{SN}} \sim 10^{52}$ erg, and a metal yield of $y \sim 0.5$, has a dramatic impact on subsequent evolution, evacuating the gas within the host halo, and preventing further star formation for about a Hubble time, ~ 300 Myr at $z \sim 10$. As the ejected metals fall back into the emerging galaxy, the central gas is enriched up to $Z \gtrsim 10^{-3.5} Z_{\odot}$ (e.g. Wise & Abel 2008; Greif et al. 2010). On the other hand, the recovery from the feedback of less massive Pop III stars ($\lesssim 40 M_{\odot}$), followed by CCSNe with $E_{\text{SN}} \sim 10^{51}$ and $y = 0.05$, was rather prompt, with recovery timescales of only a few ~ 10 Myr (Jeon et al. 2014b). Such prompt recovery allowed the first galaxies to experience multiple episodes of star formation prior to their assembly (Ritter et al. 2012, 2014). Related to this weakened feedback, the star-forming gas inside the first galaxies was possibly enriched by multiple SNe. The resulting metal enrichment was sufficient to affect a transition of the star formation mode from Pop III to normal, Population II (Pop II) stars. Thus, regions that hosted moderate mass Pop III stars would locally undergo the transition to (low-mass dominated) Pop II star formation earlier on.

The minimum (“critical”) metallicity for the Pop III/Pop II transition depends on which cooling is responsible for the gas fragmentation (e.g. Omukai 2000; Bromm et al. 2001; Schneider et al. 2002; Bromm & Loeb 2003b; Omukai et al. 2005; Schneider & Omukai 2010; Schneider et al. 2012; Chiaki et al. 2014; Ji et al. 2014). Fine-structure line cooling, mainly via C II and O I, above $Z \sim 10^{-3.5} Z_{\odot}$, leads to vigorous fragmentation of the gas cloud, giving rise to the formation of stellar clusters. Further fragmentation can be achieved at very high densities, $n_{\text{H}} \gtrsim 10^{16} \text{ cm}^{-3}$, via dust continuum cooling if the initial gas-to-dust ratio exceeds $D_{\text{crit}} = [2.6 - 6.3] \times 10^{-9}$ (Schneider et al. 2012; Chiaki et al. 2014). Globally, the Pop III/Pop II transition is a gradual process, as the ejected metals are brought back into virialized host haloes, keeping a large fraction of the IGM still pristine. Therefore, those two populations co-existed, such that Pop III star formation was still possible even at $z \sim 6$ (e.g. Trenti et al. 2009; Maio et al. 2010, 2011; Scannapieco et al. 2003; Wise et al. 2012; Johnson et al. 2013).

Here, we present the results of a cosmological zoom-in, high-resolution radiation-hydrodynamics simulation, following the first galaxy assembly process from first principles. We consider realistic descriptions of Pop III/Pop II star formation, photoionization and photoheating from stars, the mechanical and chemical feedback from PISNe and CCSNe, and the X-ray feedback from accreting BHs and HMXBs. Guided by the results from recent investigations of primordial star formation, we in particular explore the implica-

tions of a somewhat less top-heavy Pop III IMF, with a characteristic mass of a few $\sim 10 M_{\odot}$, giving rise to a large fraction of CCSNe rather than PISNe.

The outline of the paper is as follows. Our numerical methodology is described in Section 2, and the simulation results are presented in Section 3. Finally, our main findings are summarized in Section 4. For consistency, all distances are expressed in physical (proper) units unless noted otherwise.

2 NUMERICAL METHODOLOGY

2.1 Gravity, hydrodynamics, and chemistry

We have performed our simulations using a modified version of the N -body/TreePM Smoothed Particle Hydrodynamics (SPH) code GADGET (Springel et al. 2001; Springel 2005). The initial conditions within a cubic volume 1 comoving Mpc on a side are generated by assuming a Λ CDM cosmology with a matter density parameter of $\Omega_m = 1 - \Omega_{\Lambda} = 0.3$, baryon density $\Omega_b = 0.04$, present-day Hubble expansion rate $H_0 = 70 \text{ km s}^{-1} \text{ Mpc}^{-1}$, spectral index $n_s = 1.0$, and normalization $\sigma_8 = 0.9$. The initial conditions are hierarchically refined by a consecutive zoom-in technique, rendering the masses of dark matter (DM) and SPH particles in the highest resolution region with an approximate linear size of 300 comoving kpc $m_{\text{DM}} \approx 33 M_{\odot}$ and $m_{\text{SPH}} \approx 5 M_{\odot}$, respectively. We adopt the gravitational softening length $\epsilon_{\text{soft}} = 70$ comoving pc for both DM and baryonic particles. We start our simulations at $z \approx 100$ and follow the cosmic evolution of the DM and gas until the assembly process of the first galaxy has been completed at $z \approx 10$.

We consider all relevant primordial chemistry and cooling processes. Specifically, we include H and He collisional ionization, excitation and recombination cooling, bremsstrahlung, inverse Compton cooling, and collisional excitation cooling of H_2 and HD. The code self-consistently solves the non-equilibrium chemistry for 9 abundances (H, H^+ , H^- , H_2 , H_2^+ , He, He^+ , He^{++} , and e^-), as well as for the three deuterium species D, D^+ , and HD. Additionally, metal-enriched gas can also be cooled by metal species, specifically C, O, and Si, with solar relative abundances. For the metal cooling rates, we adopt the results of Glover & Jappsen (2007). The chemical network comprises the key species, C, C^+ , O, O^+ , Si, Si^+ and Si^{++} . We assume that all the metals are in gas phase atoms or ions, and thus we do not consider dust cooling as the gas densities explored in this work are far below the threshold value above which it starts to become important.

2.2 Star formation physics

2.2.1 Population III

For the star formation, we do not form stars by following the evolution from the initial protostars to the final mass (e.g. Hirano et al. 2014), rather we adopt a sink algorithm (Johnson & Bromm 2006), where stars are represented by sink particles. Once a gas particle exceeds the threshold density, $n_{\text{H,max}} = 10^4 \text{ cm}^{-3}$, the highest-density SPH particle is converted into a collisionless sink particle, subsequently accreting neighboring gas particles until the mass of the Pop III star is reached. The masses of Pop III stars are randomly sampled from an IMF with a functional form of

$$\frac{dN}{d \ln M} \propto M^{-1.3} \exp \left[- \left(\frac{M_{\text{char}}}{M} \right)^{1.6} \right], \quad (1)$$

where $M_{\text{char}} = 20 M_{\odot}$ is the characteristic mass. Above M_{char} , it behaves as a Salpeter-like IMF, but is exponentially cutoff below that mass (e.g. Chabrier 2003; Wise et al. 2012). Once a sink particle forms, we prevent the subsequent star formation in a sphere with radius 30 pc centered on the sink particle for ~ 1 Myr. This is because it takes time for the hydrodynamical shocks with a velocity ~ 30 km/s, generated by photoheating to sweep up and evacuate the central gas, reducing the central gas densities. Without such temporary suppression in star formation, multiple stars might form at the same location at the same time. This would correspond to fragmentation within the SPH smoothing kernel, which is not resolved, and would thus be physically unreliable. We allow sink particles to merge once their distance falls below 1 pc, similar to the baryonic resolution scale $l_{\text{res}} \equiv [(3X M_{\text{res}})/(4\pi n_{\text{H,max}} m_{\text{H}})]^{1/3} \approx 0.5$ pc, where $X = 0.76$ is the hydrogen mass fraction. Here, the baryonic mass resolution is $M_{\text{res}} \equiv N_{\text{ngb}} m_{\text{SPH}} \approx 240 M_{\odot}$, where $N_{\text{ngb}} = 48$ is the number of particles in the SPH smoothing kernel (Bate & Burkert 1997). The new positions and velocities of the merged sinks are computed by mass-weighted averaging.

2.2.2 Population II

Pop II stars are formed out of the gas cloud which is metal-enriched by the previous generation of stars. The star formation recipe is similar to that of Pop III star formation except for one more condition: if the metallicity of a gas particle, eligible for star formation, exceeds the characteristic metallicity, $Z_{\text{crit}} = 10^{-3.5} Z_{\odot}$, for the transition from Pop III to Pop II, we assume that a newly formed sink particle represents a Pop II star cluster. Therefore, once a SPH particle satisfies those two criteria, $n_{\text{H,max}} = 10^4 \text{ cm}^{-3}$ and $Z_{\text{crit}} = 10^{-3.5} Z_{\odot}$, we immediately create an effective sink particle with a mass of $M_{\text{Pop II}} = 500 M_{\odot}$, by accreting surrounding gas particles. The mass of a Pop II cluster $M_{\text{Pop II}} = 500 M_{\odot}$ is chosen to host one massive star $\sim 20 M_{\odot}$, given a Salpeter IMF, $dN/d \log m \approx m^{-\alpha}$, with a slope $\alpha = 1.35$, which is from Schaerer (2003) where they provide photoionization rates derived from an assumed IMF for a Pop II cluster. In the presence of a $20 M_{\odot}$ star, further star formation inside of the cluster after the initial burst is truncated by the photoheating of the star (Safranek-Shrader et al. 2014b).

2.3 Feedback physics

2.3.1 Photoionization feedback

Once a star forms, the star particle emits ionizing radiation over its lifetime with a black-body spectrum. We use the radiative transfer (RT) code TRAPHIC to transport ionizing photons (Pawlik & Schaye 2008, 2011). In simulations with TRAPHIC, photon packets from radiation sources are transferred along the irregular, spatially adaptive grid set by SPH particles in a photon-conserving manner through the simulation box. Thanks to a photon packet merging technique in TRAPHIC, the computational cost is independent of the number of ionizing radiation sources, which enables large simulations considering many sources, and as presented here. The RT is controlled by a set of parameters, which we choose identical to those employed in Jeon et al. (2014a), except that we here use two frequency bins, $N_{\nu} = 2$ instead of $N_{\nu} = 4$, with bounding energies located at [13.6 eV, 400 eV, 10 keV]. While the main focus of Jeon et al. (2014a) is to investigate the impact of X-rays on the gas in haloes and IGM, requiring to track high energy photons

denoted by the high characteristic frequencies, in this work we focus on the stellar feedback impact. To do so, two frequency bins, $N_\nu = 2$, are sufficient to represent the stellar spectrum. We refer the reader to the original papers (Pawlik & Schaye 2008, 2011) for further details concerning RT methods and to Jeon et al. (2014a) for the RT parameters we use in this work. The RT computation is coupled to the hydrodynamical evolution by passing the photoionization, photoheating, and photodissociation rates computed by the RT to the non-equilibrium solver for the chemical and thermal evolution of the gas.

For the ionizing photon rates of Pop III stars and their lifetimes, we employ polynomial fits (Schaerer 2003) as a function of initial mass of a star, $\log_{10} \dot{N}_{\text{ion}} = 43.61 + 4.90x - 0.83x^2$ and $\log_{10} t_* = 9.785 - 3.759x + 1.413x^2 - 0.186x^3$, respectively, where $x = \log_{10}(M_{\text{Pop III}}/M_\odot)$. For Pop II clusters, we use the value from Schaerer (2003) that provides the properties of integrated stellar populations at various metallicities. In particular, we fixed the ionizing photon rate for the initial ~ 3 Myr at $\dot{N}_{\text{ion}} = 10^{47} \text{ s}^{-1} M_\odot^{-1}$, which is derived by averaging over a Salpeter IMF with a slope of $\alpha = 1.35$ and a metallicity of $Z = 5 \times 10^{-3} Z_\odot$ in the mass range of $[1 M_\odot, 150 M_\odot]$. For the following evolution of the rates, we use a polynomial fit (Schaerer 2003), $\log_{10} \dot{N}_{\text{ion}} = 48.13 - 0.42t + 0.01t^2 \text{ s}^{-1} M_\odot^{-1}$, where t is the elapsed time in Myr after Pop II cluster formation. The emission from Pop II stars lasts for 20 Myr, corresponding to the typical lifetime of OB stars in the cluster.

In addition to the ionizing radiation from individual Pop III stars and Pop II clusters, we also track the Lyman-Werner (LW) radiation from both populations that dissociates molecular hydrogen (H_2) and deuterated hydrogen (HD). This is treated in the optical thin limit with a self-shielding correction (Wolcott-Green et al. 2011). The rate at which LW photons are emitted by Pop III stars is fit using $\log_{10} \dot{N}_{\text{LW}} = 44.03 + 4.59x - 0.77x^2$ (Schaerer 2002). We only allow stars to form within the highly resolved region corresponding to a linear size of ≈ 300 comoving kpc and do not follow the propagation of photons outside the region. For simplicity, we do not consider a global UV background here.

2.3.2 Supernova feedback

The SN explosion energy is inserted as thermal energy into the neighboring SPH particles, $\bar{N}_{\text{neigh}} = 32$, a subset of the particles within the SPH smoothing kernel, N_{neigh} , around a sink particle. To ensure high accuracy and energy conservation, we use a timestep-limiter, with which the ratio of timesteps of neighboring SPH particles cannot be larger than 4 (Saitoh & Makino 2009, Durier & Dalla Vecchia 2012). Additionally, using a timestep-updater, implemented by Durier & Dalla Vecchia (2012), all neighboring particles, \bar{N}_{neigh} , around an exploding sink particle become active particles at the time of SN energy injection, enabling an immediate hydrodynamical response.

At the end of a Pop III star's lifetime, the fate of the Pop III star is determined by its initial mass. For instance, Pop III stars with masses between $9 M_\odot$ and $40 M_\odot$ are expected to end their lives as conventional core collapse SNe. Here, we use the fixed CCSN energy of $E_{\text{SN}} = 10^{51}$ ergs and metal yield, $y = 0.05$, for Pop III progenitors. We should mention that the CCSN explosion energies and the metal yields can vary depending on the progenitor's mass (e.g. Heger & Woosley 2010). In particular, under the existence of rotation of Pop III progenitor in a mass range of $25 - 40 M_\odot$, a much stronger explosion may be expected, likely resulting in a hypernova (e.g. Fryer & Heger 2000; Nomoto et al. 2006). However,

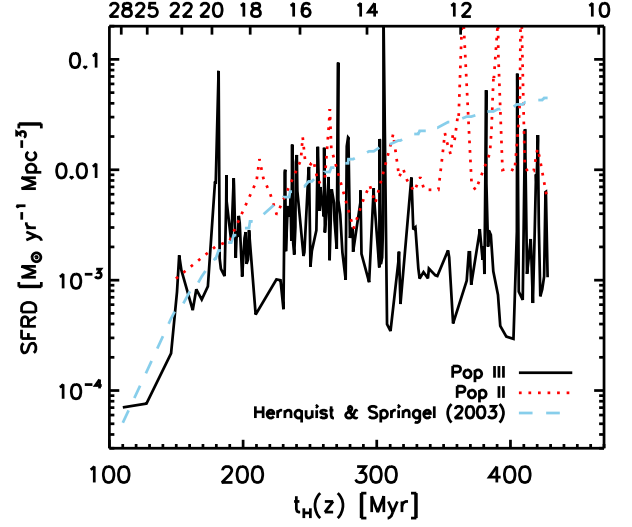


Figure 1. The history of comoving star formation rate density (SFRD) in the simulated region for Pop III (black solid line) and Pop II (red dotted line) stars. For comparison, we also show the analytic fitting formula, derived by Hernquist & Springel (2003), for higher-mass systems where atomic cooling is active (light blue-dashed line). Earlier on, at $z > 13$, Pop III star formation dominates, but as the gas is metal-enriched, the Pop II mode becomes dominant below $z \approx 13$.

due to the uncertainty in the degree of spin of Pop III stars, which is subject to stellar winds, gravitational and hydromagnetic instabilities (e.g. Stacy et al. 2011), we only consider conventional CCSNe by fixing the explosion energy and metal yield.

For the highly energetic PISNe from Pop III stars with masses in the range of $140 M_\odot \lesssim M_* \lesssim 260 M_\odot$ (Heger & Woosley 2002), we adopt the SN energy of 10^{52} ergs and $y = 0.5$. Out of a Pop II cluster with a mass of $500 M_\odot$, a total of 9 stars more massive than $8 M_\odot$, above which the stars are eligible to explode as CCSNe, are expected to form. We simultaneously trigger 9 SNe explosions at the end of the lifetime of a Pop II cluster, injecting an energy of 9×10^{51} ergs with an IMF-averaged effective metal yield $y_{\text{eff}} = 0.005$ onto the neighboring particles around the Pop II sink particle.

Initially, the metals from SN explosions are evenly distributed among the neighboring SPH particles, implying initial metallicities,

$$Z_i = \frac{m_{\text{metal},i}}{m_{\text{SPH}} + m_{\text{metal},i}}, \quad (2)$$

where $m_{\text{metal},i} = M_* y / \bar{N}_{\text{neigh}}$ for Pop III stars and $m_{\text{metal},i} = M_{\text{Pop II}} y_{\text{eff}} / \bar{N}_{\text{neigh}}$ for Pop II clusters. The lack of mass flux between SPH particles means that metals are transported ballistically in an SPH scheme (e.g. Wiersma et al. 2009). Physically, the mixing of metals is achieved through an unresolved turbulent cascade from large scales to small scales, which is unresolved. Therefore, often, a metal mixing is implemented by subgrid models in which physical processes below the smallest resolved scale are determined by physical quantities at resolved scales (e.g. Schmidt & Federrath 2011). We adopt a diffusion-based method implemented by Greif et al. (2009) which assume that the mixing efficiency on unresolved scales is determined by the physical properties on the scale of the SPH smoothing kernel (Klessen & Lin 2003). Consequently, the metal diffusion rate is set by the local diffusion coefficient, $D = 2 \rho \tilde{v} \tilde{l}$, where the length scale, \tilde{l} , is comparable to the

smoothing length of the SPH kernel, $\tilde{l} = h$, and ρ is the gas density. The velocity dispersion within the kernel, \tilde{v} , is given by

$$\tilde{v}_i^2 = \frac{1}{N_{\text{ngb}}} \sum_j |v_i - v_j|^2. \quad (3)$$

Here, v_i and v_j are the velocities of particles i and j within the kernel.

2.3.3 Black hole feedback

Pop III stars with masses between $40 M_\odot$ and $140 M_\odot$, or larger than $260 M_\odot$ will directly collapse into BHs (Heger et al. 2003). The BHs then grow by Bondi-Hoyle accretion (Bondi & Hoyle 1944), assuming that a fraction $\epsilon = 0.1$ of the accreted mass is converted into ionizing radiation. Such stellar mass BHs accreting diffuse gas are called miniquasars (Kuhlen & Madau 2005). The ionizing luminosities of miniquasars are determined by normalizing the total accretion luminosity

$$L_{\text{BH}} \equiv \int_0^{10 \text{keV}/h_{\text{P}}} L_\nu d\nu = \frac{\epsilon}{1-\epsilon} \dot{M}_{\text{BH}} c^2, \quad (4)$$

where h_{P} is Planck's constant and c is the speed of light. The BH (sink) particles grow in mass by accreting surrounding gas according to the accretion rate, $\dot{M}_{\text{BH}} = (1 - \epsilon)\dot{M}_{\text{acc}}$, which is computed as

$$\dot{M}_{\text{acc}} = \frac{4\pi G^2 M_{\text{BH}}^2 \rho}{(c_s^2 + v_{\text{rel}}^2)^{3/2}}. \quad (5)$$

Here, c_s is the sound speed, ρ the gas density, M_{BH} the BH mass, and v_{rel} the relative velocity of the BH to the surrounding gas. Note that Bondi-Hoyle accretion is thus a numerical input, or recipe, and not an independent simulation result. The estimated rate is an upper limit. In reality, the true accretion rates are likely smaller than the nominal Bondi-Hoyle value, if feedback from radiation pressure is considered (e.g. Milosavljević et al. 2009a,b; Park & Ricotti 2012). In addition, at later time as the gas in an atomic cooling halo becomes turbulent, the vorticity of the turbulent gas can reduce the accretion onto the BH (Krumholz et al. 2005). Motivated by observations at low redshifts, we take the same form of a spectral energy distribution of the emerging radiation from an accreting single black hole, which is characterized by a thermal multi-color disk (e.g. Pringle 1981; Mitsuda et al. 1984) at frequencies lower than $0.2 \text{ keV}/h_{\text{P}}$ and a non-thermal power law component at higher frequencies (e.g. Kuhlen & Madau 2005). For the details, we refer the reader to Jeon et al. (2014a).

Further, we assume that half of the black holes are formed in a binary system and then every third of those evolve into a HMXB after the primary turned into a BH (Power et al. 2009). For the HMXB phase of duration $\Delta t_{\text{HMXB}} = 2 \text{ Myr}$, corresponding to the typical main-sequence lifetime of the donor stellar companion (e.g. Belczynski et al. 2012), we assume an HMXB luminosity equal to the Eddington luminosity,

$$L_{\text{HMXB}} \equiv \int_0^{10 \text{keV}/h_{\text{P}}} L_\nu d\nu = L_{\text{Edd}} \quad (6)$$

$$= 1.4 \times 10^{40} \text{ erg s}^{-1} \left(\frac{M_{\text{BH}}}{100 M_\odot} \right), \quad (7)$$

corresponding to accretion of gas from the companion at a rate $2.2 \times 10^{-6} M_\odot \text{ yr}^{-1} (M_{\text{BH}}/100 M_\odot)$. The X-ray radiation is followed using RT. We also take into account the secondary ionizations, which are mainly done by high energy electrons left behind

the first ionizations of hydrogens by hard energy photons emitted from an accreting BH or a HMXB. We use the energy dependent fits to the secondary ionization and heating fractions provided by Ricotti et al. (2002).

3 SIMULATION RESULTS

In the following, we present our results. First, in Section 3.1, we discuss the global properties of the IGM and of haloes within the highly resolved region and their evolution to $z \approx 10$. In Section 3.2, we focus on the assembly process of the central halo hosting the emerging galaxy. Then, based on the physical quantities derived from this galaxy, we compare the properties of the first galaxy with those of the local counterparts in Section 3.3. Finally, in Section 3.4, we discuss the detectability of the simulated first galaxy.

3.1 Global evolution

3.1.1 Star formation history

In the simulation, the first Pop III star, with a randomly assigned mass of $100 M_\odot$, forms at $z \approx 28$ out of the primordial gas in a minihalo with mass $M_{\text{vir}} \sim 5 \times 10^5 M_\odot$. After its short lifetime of 2.7 Myr, the star ends up as a BH in a binary system, forming a HMXB. Over a brief interval of $\Delta t_{\text{HMXB}} = 2 \text{ Myr}$, X-rays emitted from the HMXB further heat the surrounding gas, which was already heated to $\sim 10^4 \text{ K}$ by the Pop III progenitor, and they heat the distant IGM to a few $\sim 10^3 \text{ K}$. At $z \approx 23$, the first Pop II star formation event takes place in metal-enriched gas, which was previously polluted by a Pop III star, whose mass of $20 M_\odot$ was again randomly drawn from the underlying IMF Pop III star. The time delay between the onset of second-generation, Pop II, star formation and the death of the $20 M_\odot$ Pop III star is $\sim 16 \text{ Myr}$, consistent with our earlier study (Jeon et al. 2014b). By the end of the simulation at $z \approx 10.5$, a total of $N_{\text{Pop II}} = 65$ Pop II clusters and $N_{\text{Pop III}} = 183$ individual Pop III stars has formed, with 128, 2, 44, and 11 Pop III stars ending their lives as CCSNe, PISNe, BHs, and HMXBs, respectively.

Fig. 1 shows the comoving star formation rate density (SFRD) for the Pop III individual stars and the Pop II clusters. During the initial 50 Myr, only Pop III stars exist. However, once metal pollution commences by Pop III SNe, the metallicity of the gas increases to trigger the transition of the star formation mode from Pop III to Pop II. Therefore, at $z \lesssim 23$, two star formation modes coexist over the next $\sim 350 \text{ Myr}$. As the dense gas available for star formation gets metal-enriched, the dominant star formation mode changes from Pop III to Pop II. Accordingly, the SFRD for Pop II stars begins to increase and reaches a few $\sim 10^{-2} M_\odot \text{ yr}^{-1} \text{ Mpc}^{-3}$ at $z \approx 14$. On the contrary, Pop III star formation starts to decline from $\sim 7 \times 10^{-3} M_\odot \text{ yr}^{-1} \text{ Mpc}^{-3}$ at $z \approx 14$ to a few $\sim 10^{-3} M_\odot \text{ yr}^{-1} \text{ Mpc}^{-3}$ at $z \approx 10.5$ as the amount of dense pristine gas decreases.

It is noteworthy that the SFRDs measured in the simulation are very episodic rather than continuous. This episodic, bursty star formation is mainly caused by a stellar feedback cycle: dense gas inside a halo is evacuated by photoheating from stars, the subsequent SN blastwave, or both, rendering it gas-starved for a certain time, until fresh gas is provided through smooth accretion or mergers with other haloes. Such self-regulated star formation on short timescales is also exhibited by simulations of more massive galaxy

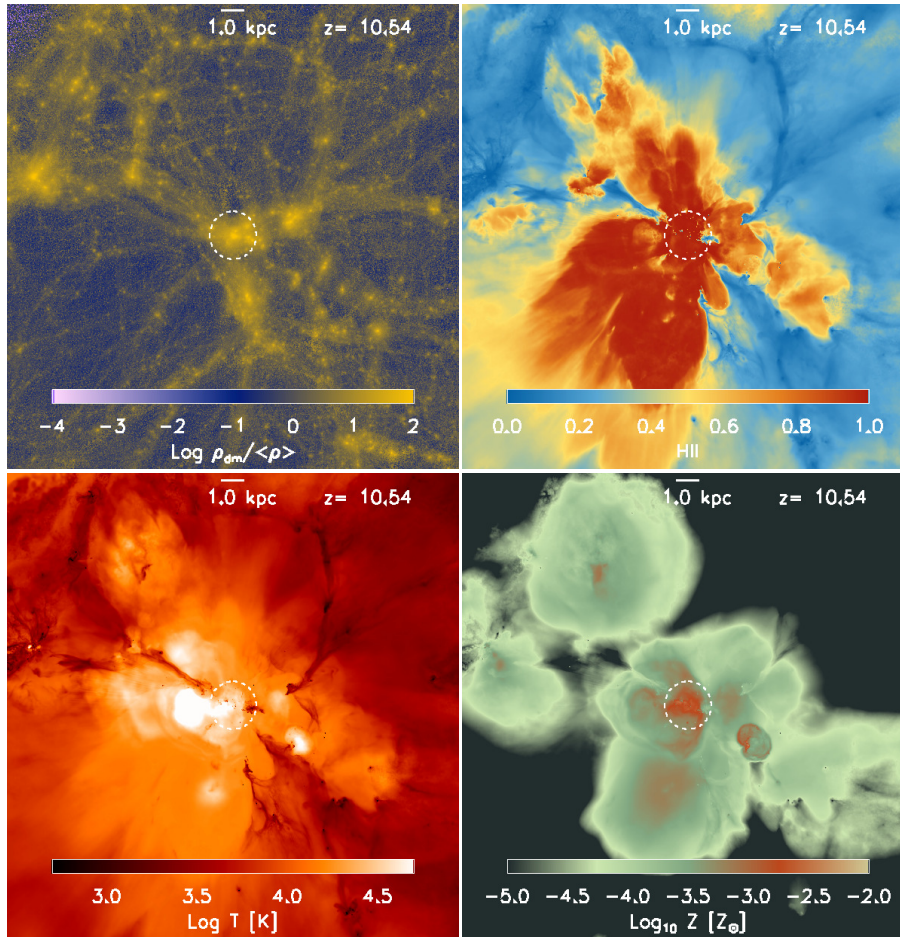


Figure 2. Morphology in the highly resolved region at $z \approx 10.5$. *Clockwise from upper left:* Dark matter overdensity, H II fraction, gas metallicity, and gas temperature, averaged along the line of sight within the central ≈ 350 kpc (comoving). The central white circles denote the size of the virial radius, $r_{\text{vir}} \approx 1.1$ kpc, of the emerging target galaxy. The target halo grows in mass through mergers with neighboring haloes and accretion along the filaments of the cosmic web. The gas in haloes that are undergoing star formation is evacuated and heated, and metal-enriched by stellar feedback. The main metal contributors to the diffuse IGM are two energetic PISNe, formed at $z \approx 16$ and $z \approx 15.5$, and ejecting a total of $\sim 160 M_{\odot}$ in heavy elements into the IGM.

formation (Hopkins et al. 2014), where stellar feedback, i.e. photoheating, SNe, winds, and radiation pressure, is taken into account with approximate sub-grid prescriptions. For comparison, we overplot the analytic fitting formula, derived by Hernquist & Springel (2003), for higher-mass systems, where atomic cooling is active, which agrees well with the SFRD for Pop II stars predicted by our simulation. We, however, should note that the SFRDs both for Pop III and Pop II stars are higher than those computed in the adaptive mesh refinement simulation of Wise et al. (2012) by a factor of ~ 5 . The reason for this is the biased nature of our zoomed, high-resolution region, focusing on a small volume and omitting under-dense void regions, which results in enhanced star formation activity compared to the cosmic mean.

3.1.2 Global impact of stellar feedback

Fig. 2 shows images of the dark matter overdensity, ionized hydrogen fraction, gas temperature, and gas metallicity at $z \approx 10.5$ in the high-resolution region, corresponding to ~ 350 comoving kpc across, centered on the site of the emerging target galaxy. The virial radius of the halo hosting the target galaxy, depicted as the white dashed circle in Fig. 2, grows over time from $r_{\text{vir}} \approx 100$ pc at

$z = 28$ to $r_{\text{vir}} \approx 1.1$ kpc at $z = 10.5$. Correspondingly, the halo grows in mass from $5 \times 10^5 M_{\odot}$ to $8 \times 10^7 M_{\odot}$. Both the gas inside haloes and in the diffuse IGM are subject to a variety of heating sources, such as UV radiation from Pop III and Pop II stars, X-rays from accreting BHs and HMXBs, and thermalized SN explosion energy. The temperature inside H II regions reaches $T \approx 10^4$ K by stellar photoionization heating, and further increases to $10^7 - 10^8$ K due to SN shock heating. Such high-temperature gas is primarily cooled via inverse Compton cooling off the cosmic microwave background (CMB) and free-free emission to 10^6 K, and then H and He recombination cooling begins to dominate at the lower temperature of $10^4 - 10^6$ K (Greif et al. 2007).

In order to disentangle the contribution of radiation sources to ionization and heating, in Fig. 3 we compare the ionizing photon rates from Pop III stars, Pop II stars, and HMXBs. While the ionizing photons from Pop III stars are responsible for ionizing the gas at high redshifts $z \gtrsim 13$, the contribution from Pop II stars becomes competitive at later times. On the other hand, the contribution from a handful of HMXBs is negligible owing to their rarity and their short lifetime, $\Delta t_{\text{HMXB}} = 2$ Myr, although the latter quantity is very uncertain and may be larger. In Jeon et al. (2014a), the impact of X-rays from HMXBs on star formation was similarly negligible,

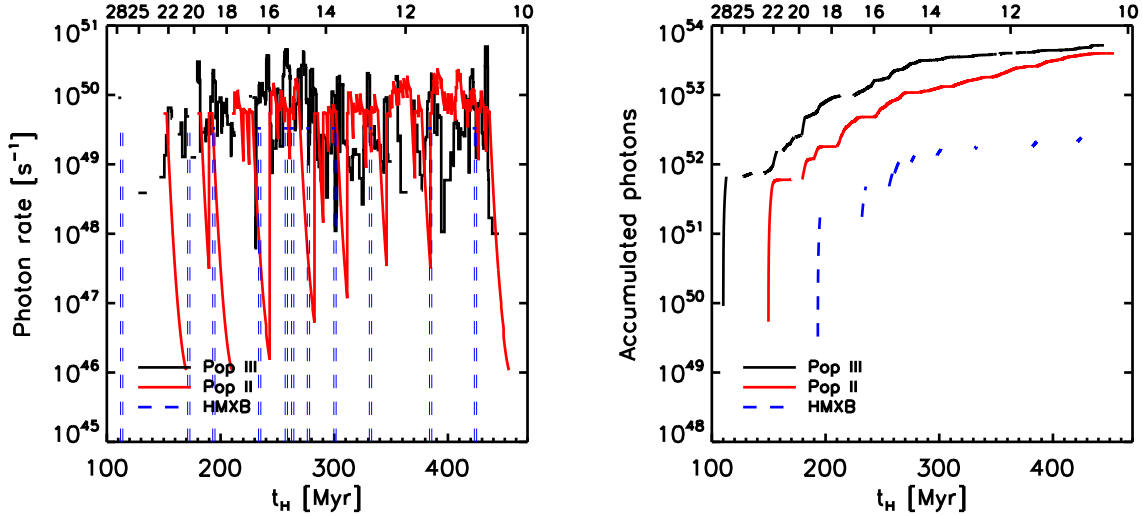


Figure 3. The evolution of ionizing photon rates (*left*) and total accumulated photons (*right*) from the Pop III stars, Pop II clusters, and HMXBs. The contribution from Pop III stars dominates the total ionizing photon budget up to $z \approx 10.5$, but Pop II clusters are about to overtake it, as the global star formation mode changes to Pop II star formation. The total photon production from the 11 HMXBs formed during the run is negligible, mainly due to our assumption here of a very brief interval of 2 Myr, over which the X-ray source is active. This interval, however, is uncertain, and could be larger. If so, the relative HMXB contribution to the ionizing photon budget could be more significant.

while the effect of X-ray heating in the diffuse IGM was significant, smoothing out small-scale structures. This smoothing effect is less prominent in the current simulation, which hosts only a single HMXB by $z \approx 18$, instead of the 8 sources present at that time in our previous study.

We assess the impact of the stellar feedback on individual haloes by using the SUBFIND halo finder (Springel et al. 2001) to identify haloes from the highly-refined region in the simulated volume, allowing us to investigate their gas, stellar, and metal properties. Each circle in Fig. 4 marks the mass-weighted average of the corresponding stellar or gas properties inside the virial sphere, which is centered on the most bound DM particle of the halo, and bounded by radii where the DM density is 200 times higher than the mean density of the Universe. Star formation takes place only in haloes more massive than $M_{\text{vir}} = 5 \times 10^5 M_{\odot}$, below which the haloes are not massive enough to satisfy the condition $t_{\text{cool}} < t_{\text{ff}}$, where t_{cool} and t_{ff} are the cooling time and the free-fall time, respectively, for the gas to cool and form stars (e.g. Tegmark et al. 1997; Bromm et al. 2002).

Fig. 4 shows the gas properties of the extracted haloes at $z \approx 10.5$, including the baryon fraction, the total mass of Pop III BH remnants and Pop II low-mass (long-lived) stars, the highest gas density achieved, and the average metallicity of the gas in the halo. Photoheating and SNe drive the gas out of the haloes, lowering the baryon fraction below the cosmic mean (upper-left panel of Fig. 4). Among the haloes more massive than $10^6 M_{\odot}$ at $z \approx 10.5$, about 40%, corresponding to 7 out of 17 haloes (blue circles in Fig. 4), experience photoheating and SN blastwave heating by both Pop III stars and Pop II clusters. Specifically, the three most massive haloes, ($M_{\text{vir}} \sim 7 \times 10^7 M_{\odot}$, $\sim 3 \times 10^7 M_{\odot}$, $\sim 2 \times 10^7 M_{\odot}$) at $z \approx 10.5$ have experienced (32, 9, 7) Pop III SNe and (28, 2, 3) SNe from Pop II clusters. The gas fractions of these haloes at $z \approx 10.5$ are 5.1%, 3.3%, and 3%, respectively. For lower-mass haloes, on the other hand, the scatter in the gas fraction is much more substantial, due to their susceptibility to negative stellar feedback in the shallow potential wells. Those haloes are more likely to

lose their gas once they undergo star formation, and it takes longer for the ejected gas to be re-incorporated.

About 35% of the haloes larger than $M_{\text{vir}} \gtrsim 10^6 M_{\odot}$, denoted as red circles, only host Pop III stars. Most of them experience subsequent CCSN explosions, whereas 2 haloes host a rare PISN. The effect of a PISN is much more disruptive than that of a CCSN. As an example, the third heaviest halo hosts a $160 M_{\odot}$ PISN at $z = 16$, when its mass reaches $M_{\text{vir}} \sim 10^7 M_{\odot}$. This hyper-energetic explosion effectively evacuates the gas within the halo, lowering the baryon fraction by an order of magnitude, from $f_{\text{bar}} = 0.088$ at $z = 16$ to $f_{\text{bar}} = 0.0046$ at $z = 13.7$. Subsequently, the halo gas begins to be replenished through accretion of both the ejected metal-enriched gas and fresh primordial gas along the cosmic filaments, such that at the end of the simulation the baryon fraction again reaches $f_{\text{bar}} = 0.03$. Despite the gas recovery, however, any further star formation inside the halo has been completely suppressed since $z = 16$.

Haloes with $M_{\text{vir}} \lesssim 10^8 M_{\odot}$, corresponding to the mass range considered in this work, are susceptible not only to the local stellar feedback inside the host itself, but also to the external global UV background that also photoheats the gas in their shallow potential wells, reducing the baryon fraction. For comparison, we overplot a fit (dotted line the upper-left panel of Fig. 4) that describes how the baryon fraction is affected by reionization as a function of halo mass and redshift (Gnedin 2000; Okamoto et al. 2008):

$$f_{\text{bar}}(M, z) = \langle f_{\text{bar}} \rangle \left(1 + (2^{\beta/3} - 1) \left[\frac{M}{M_c(z)} \right]^{-\beta} \right)^{-3/\beta}, \quad (8)$$

where $\langle f_{\text{bar}} \rangle$ is the cosmic mean baryon fraction, $\beta = 2$ a fitting parameter, and $M_c(z = 10) = 7 \times 10^6 M_{\odot}$ the characteristic mass, below which galaxies are strongly affected by the UV background. The gas in haloes affected by internal feedback from both Pop III and Pop II stars tends to be more strongly evacuated, compared to

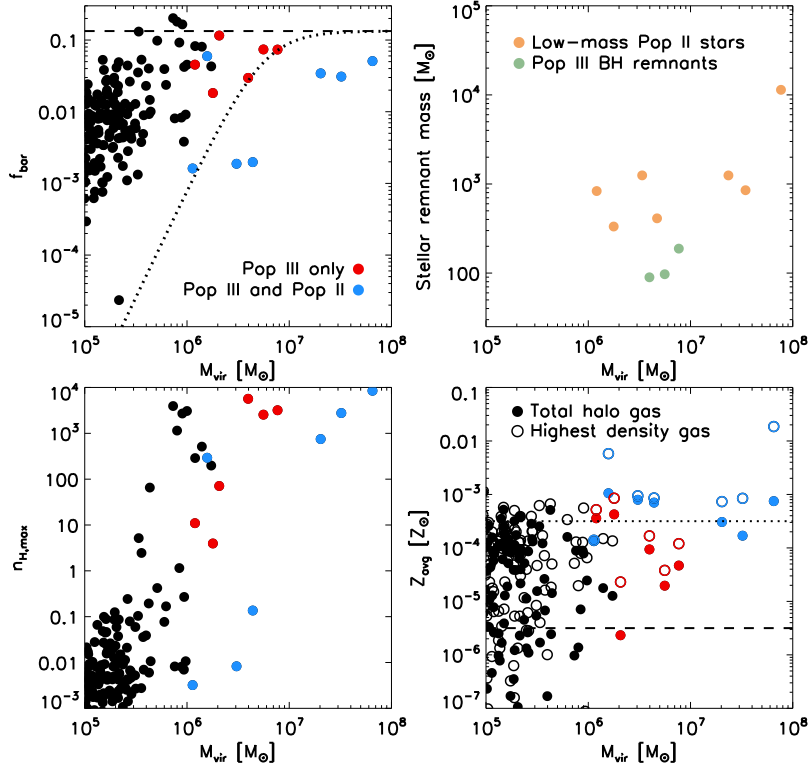


Figure 4. The properties of gas, stars, and metals in haloes at $z \approx 10.5$, extracted from the high resolution region using the SUBFIND halo finder (Springel et al. 2001). *Clockwise from upper left:* halo baryon fraction, total mass in Pop III BH remnants and long-lived (low-mass) Pop II stars, average metallicity of the total halo gas and of the high-density gas, and the maximum hydrogen number density. These properties are computed by mass-weighted averaging inside the virialized region centered on the most bound halo particle. Due to the feedback from photoheating, SNe, or both, the gas inside the haloes is significantly evacuated, giving rise to baryon fractions below the cosmic mean value (dashed horizontal line in the upper-left panel). For comparison, we also show the predicted suppression in baryon fraction due to the presence of a global, external UV background, as given in Equ. 8 (dotted line in the upper-left panel). About 46% of star-forming haloes (colored circles) only host a single or a few Pop III stars (red circles), whereas the remainder hosts both populations (blue circles). The haloes more massive than $M_{\text{vir}} = 10^6 M_{\odot}$ are substantially metal-enriched, giving rise to an average metallicity above $Z = 10^{-5.5} Z_{\odot}$. The dotted and dashed horizontal lines in the bottom right panel denote the critical metallicity for the Pop III/Pop II transition, $Z_{\text{crit}} = 10^{-3.5} Z_{\odot}$ and $Z_{\text{crit,dust}} = 10^{-5.5} Z_{\odot}$, corresponding to metal fine-structure line cooling and dust continuum cooling, respectively. Depending on the choice of critical metallicity, the timing of the Pop III to Pop II transition in a given halo can vary.

the external UV background case, whereas f_{bar} in haloes hosting only Pop III stars is less severely attenuated.

The average gas metallicity in the haloes with $M_{\text{vir}} \gtrsim 10^6 M_{\odot}$ lies between $Z_{\text{avg}} = 10^{-5} - 10^{-3} Z_{\odot}$. The metal-enrichment in the individual haloes is mainly achieved by CCSNe, because the relatively low characteristic mass, $M_{\text{char}} = 20 M_{\odot}$, for the Pop III IMF results in only two PISNe during the run. When the $160 M_{\odot}$ PISN is triggered, the surrounding gas is immediately polluted to an average of $Z = 4 \times 10^{-3} Z_{\odot}$. However, those heavy elements are quickly driven out beyond the virial radius of the host halo. After 50 Myr, the ejected metals start to fall back as gas is accreted, and the average gas metallicity reaches $Z = 3 \times 10^{-4} Z_{\odot}$ in the halo with a mass of $M_{\text{vir}} \approx 2 \times 10^7 M_{\odot}$ at $z \approx 10.5$. This agrees with the results by Wise et al. (2012), where they found that for haloes $M_{\text{vir}} > 3 \times 10^7 M_{\odot}$, all haloes are enriched above $[Z/H] > -4$. However, we should point out that the metal contributors were Pop III PISNe in their work, while the haloes at $z = 10.5$ in the current work are mainly polluted by CCSNe. At $z \approx 10.5$, if we consider all haloes with a mass above

$M_{\text{vir}} = 10^5 M_{\odot}$, only 2% of them experience in-situ star formation, while 25% of the haloes exhibit an average gas metallicity above $Z = 10^{-6} Z_{\odot}$. Thus, some of them were enriched by SNe in nearby haloes.

Given that star formation takes place in cold dense gas, specifically considering the metallicity of the densest gas in the haloes is meaningful. In the most massive three haloes, the densest gas is enriched above $Z_{\text{crit}} = 10^{-3.5} Z_{\odot}$ (see the bottom-right panel of Fig. 4), indicating that Pop II stars are expected to form out of the gas. However, it does not necessarily imply that the haloes cease forming Pop III stars. Instead, Pop III stars may continue to form until the end of the simulation in the highest density regions, which are already metal-enriched, but possibly insufficiently so to enable Pop II star formation. The time at which the Pop III/Pop II transition occurs depends on the choice of the critical metallicity, which is still quite uncertain. For instance, the densest clouds (open circles above 10^3 cm^{-3} in the bottom-left panel of Fig. 4) in the haloes between $3 \times 10^6 M_{\odot} \lesssim M_{\text{vir}} \lesssim 10^7 M_{\odot}$ are about to form stars. Based on $Z_{\text{crit}} = 10^{-3.5} Z_{\odot}$, which is assumed in this work, some

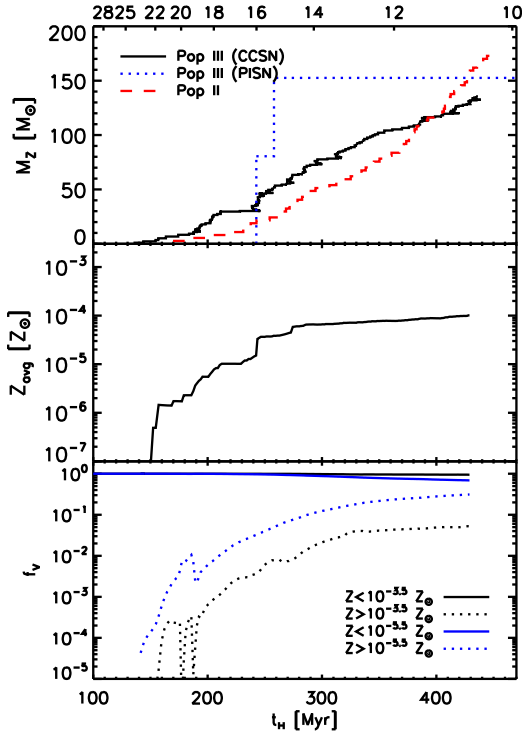


Figure 5. History of the global metal enrichment. As a series of SNe are triggered, the total amount of metals in the simulated region increases over time. Due to the large yield, $y = 0.05$, of Pop III CCSNe, compared to the effective yield of Pop II SNe, $y_{\text{eff}} = 0.005$, the former dominate, a situation that is reversed at later times, $z \lesssim 11$. In terms of the total metal budget, about 75% of the heavy elements are produced by only two PISNe owing to their extremely large yield, $y \approx 0.5$, in combination with their large progenitor mass. The average metallicity increases up to $Z_{\text{avg}} = 10^{-4} Z_{\odot}$ at $z \approx 10.5$. On the other hand, the majority of the simulated volume remains almost pristine, below $Z \lesssim 10^{-3.5} Z_{\odot}$ or $Z \lesssim 10^{-5.5} Z_{\odot}$, as shown in the bottom panel.

Pop III stars are expected to form, whereas Pop II stars would form if we adopted a critical metallicity, $Z_{\text{crit}} = 10^{-5.5} Z_{\odot}$ (dashed horizontal line in the bottom-right panel of Fig. 4), set by dust-continuum cooling (e.g. Omukai 2000; Bromm et al. 2001; Schneider et al. 2002; Bromm & Loeb 2003b; Omukai et al. 2005; Schneider & Omukai 2010; Schneider et al. 2012; Chiaki et al. 2014; Ji et al. 2014). Therefore, the latter case would give rise to an earlier transition in star formation, and would more rapidly extinguish the Pop III mode.

3.1.3 Metallicity evolution

By the end of the simulation, a total of 128 out of 183 Pop III stars end up as CCSNe and 2 stars explode as PISNe. Fig. 5 displays the resulting metal enrichment history of the simulated region. While the gas confined inside the haloes is mainly enriched by Pop III and Pop II CCSNe, the enrichment in the diffuse IGM is dominated by the rare PISN events. Indeed, although only two PISNe have occurred, they produce a total of $\sim 150 M_{\odot}$ in metals, accounting for 75% of the total metal budget at $z \approx 10.5$. Intriguingly, the optimal strategy to search for PISN-enriched material may thus be to probe the high-redshift IGM with absorption spectroscopy (Wang et al. 2012). The average mass-weighted metallic-

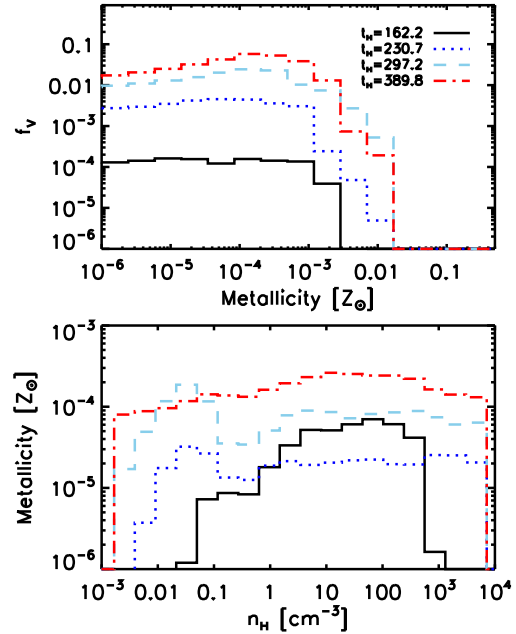


Figure 6. *Top:* Evolution of the metal-enriched volume filling fraction as a function of metallicity at four different times. As more and more regions are polluted by SNe, the volume filling fraction increases over time, but the peaks remain at the same metallicity $Z = 10^{-4} - 10^{-3} Z_{\odot}$ at all times. We normalize the volume by the total simulated volume, most of which is still pristine as shown in the bottom panel of Fig. 5. *Bottom:* The distribution of metallicity depending on the gas density. Which range of gas density is preferentially metal-enriched is sensitively determined by the gas conditions prior to a SN explosion. For a SN with a low mass progenitor, high density gas ($n_{\text{H}} = 100 \text{ cm}^{-3}$) is likely to be polluted, while the low density gas ($n_{\text{H}} = 0.1 - 0.001 \text{ cm}^{-3}$) is preferentially enriched by a SN triggered by a massive progenitor.

ity of the region increases to $10^{-4} Z_{\odot}$ at $z \approx 10.5$. However, the majority of the region is metal-enriched below the critical metallicity $Z_{\text{crit}} = 10^{-3.5} Z_{\odot}$, giving rise to a volume filling factor of $f_V \approx 0.95$ ($\lesssim 10^{-3.5} Z_{\odot}$) and $f_V \approx 0.69$ ($\lesssim 10^{-5.5} Z_{\odot}$). The volume filling fraction, f_V , is defined as

$$f_V = \frac{\sum_{\text{subset}} m_i / \rho_i}{\sum_{\text{total}} m_i / \rho_i}. \quad (9)$$

For gas that is sufficiently metal-enriched to form Pop II stars, the volume filling fraction keeps increasing and reaches $f_V \approx 0.05$ ($\gtrsim 10^{-3.5} Z_{\odot}$) and $f_V \approx 0.29$ ($\gtrsim 10^{-5.5} Z_{\odot}$) at $z \approx 10.5$.

The upper panel of Fig. 6 shows the volume filling fraction of the gas as a function of metallicity at four different characteristic times. Overall, the metal-enriched volume fraction increases over time, peaking at $Z \approx 2 - 3 \times 10^{-4} Z_{\odot}$ and declining at high metallicities $Z > 10^{-3} Z_{\odot}$. We also show the average metallicity as a function of gas density at the four selected times. The metallicity distribution sensitively depends on the gas density at the time when the SN is about to explode. The initial conditions for a SN explosion are set by the photoheating from its progenitor star. If the stellar radiative feedback is strong enough to evacuate the gas around the star, lowering the gas density to $n_{\text{H}} = 0.1 - 10^{-3} \text{ cm}^{-3}$, this low

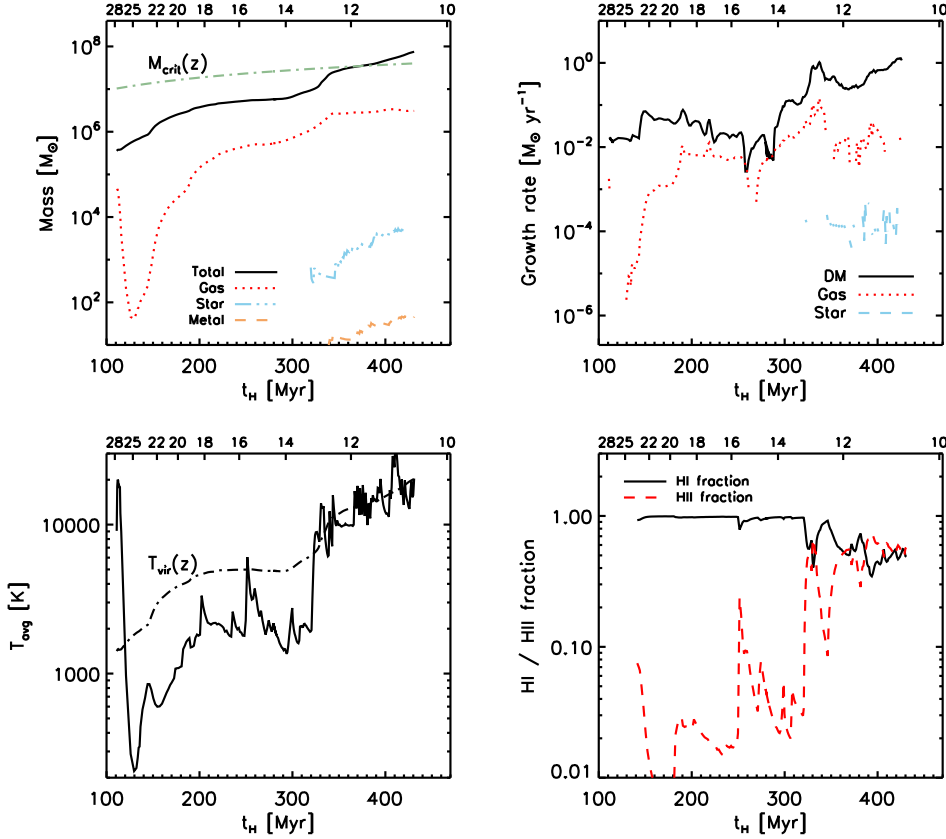


Figure 7. Assembly history of the emerging target galaxy. *Clockwise from upper left:* Mass growth of the target galaxy, growth rate of various halo components, H I/H II fractions, and the average gas temperature. Starting from $M_{\text{vir}} \approx 5 \times 10^5 M_{\odot}$ at $z \approx 28$, the galaxy grows in mass and reaches the threshold for atomic hydrogen cooling at $z \approx 11.7$. The final virial mass at the end of the simulation, $z \approx 10.5$, is $M_{\text{vir}} \sim 10^8 M_{\odot}$. The stellar content of the galaxy is dominated by Pop II, with a total mass of $M_{*} \approx 6 \times 10^3 M_{\odot}$, formed with an effective star formation rate of $\sim 10^{-4} M_{\odot} \text{ yr}^{-1}$. Through a complex interplay between metal ejection and re-accretion along the filaments of the cosmic web, roughly $\sim 40 M_{\odot}$ in metals are present inside the galaxy at the end of the simulation.

density gas is first likely to be polluted. For lower mass progenitor stars, on the other hand, due to their weaker ability of evacuating gas in their surroundings, such high density gas is preferentially enriched by the explosion.

This trend is clearly displayed in the bottom panel of Fig. 6. The progenitor mass of the first SN, triggered at $t_{\text{H}} = 133 \text{ Myr}$, is $25 M_{\odot}$. The outflow, driven by the photoheating of the $25 M_{\odot}$ Pop III star, is not strong enough to evacuate the surrounding dense gas. Therefore, the subsequent SN ejecta encounter this high density gas first, giving rise to the metallicity peak at $n_{\text{H}} = 100 \text{ cm}^{-3}$ (see solid line in the bottom panel of Fig. 6). On the contrary, sufficiently strong radiative feedback from massive progenitor stars sets the stage for the following SN explosions to occur in low-density gas, with $n_{\text{H}} = 0.01 - 0.1 \text{ cm}^{-3}$. This low density gas is then preferentially enriched, corresponding to the cases shown as dotted and dashed lines in Fig. 6. In summary, the derived trend is as follows: a SN with a low mass Pop III progenitor tends to pollute dense gas while a massive progenitor followed by a SN is more likely to enrich low density gas. This trend, however, disappears as both low and high density regions are equally polluted as SN events become more frequent.

3.2 Assembly of the first galaxy

3.2.1 Mass evolution

The first star in the Lagrangian volume of the emerging target galaxy forms at $z \approx 28$ out of the primordial gas within the main progenitor minihalo of mass $\sim 5 \times 10^5 M_{\odot}$. After its short lifetime of 2.7 Myr, the star collapses into a BH, acting as a HMXB source for the next 2 Myr. Stellar and BH feedback evacuate the gas by reducing the baryon fraction of the halo from $f_{\text{bar}} = 0.12$ at $z \approx 28$ to essentially zero at $z \approx 25$. Afterwards, the baryon fraction again increases, and at $z \approx 16$ gas densities have increased to $n_{\text{H}} = 10^4 \text{ cm}^{-3}$, thus enabling further star formation. Subsequently, the baryon fraction remains above $f_{\text{bar}} = 0.05$ throughout since $z \lesssim 16$, even in the presence of ongoing star formation, as the halo is sufficiently massive, $M_{\text{vir}} \gtrsim 5 \times 10^6 M_{\odot}$, to hold onto its gas despite feedback.

The first Pop II stars in the target halo form at $z = 13.1$ out of gas that was enriched by a $33 M_{\odot}$ Pop III star that ended its life as a CCSN, thus initiating the prolonged chemical enrichment process. Until $z = 13.3$, the halo grows in mass mainly via smooth accretion along the filaments of the cosmic web and through minor mergers. At $z \approx 13.3$, the halo experiences a major merger and doubles its mass to $2 \times 10^7 M_{\odot}$ at $z \approx 12.6$, over a time span of $\sim 25 \text{ Myr}$. The average growth rate during this period is $\dot{M} \approx$

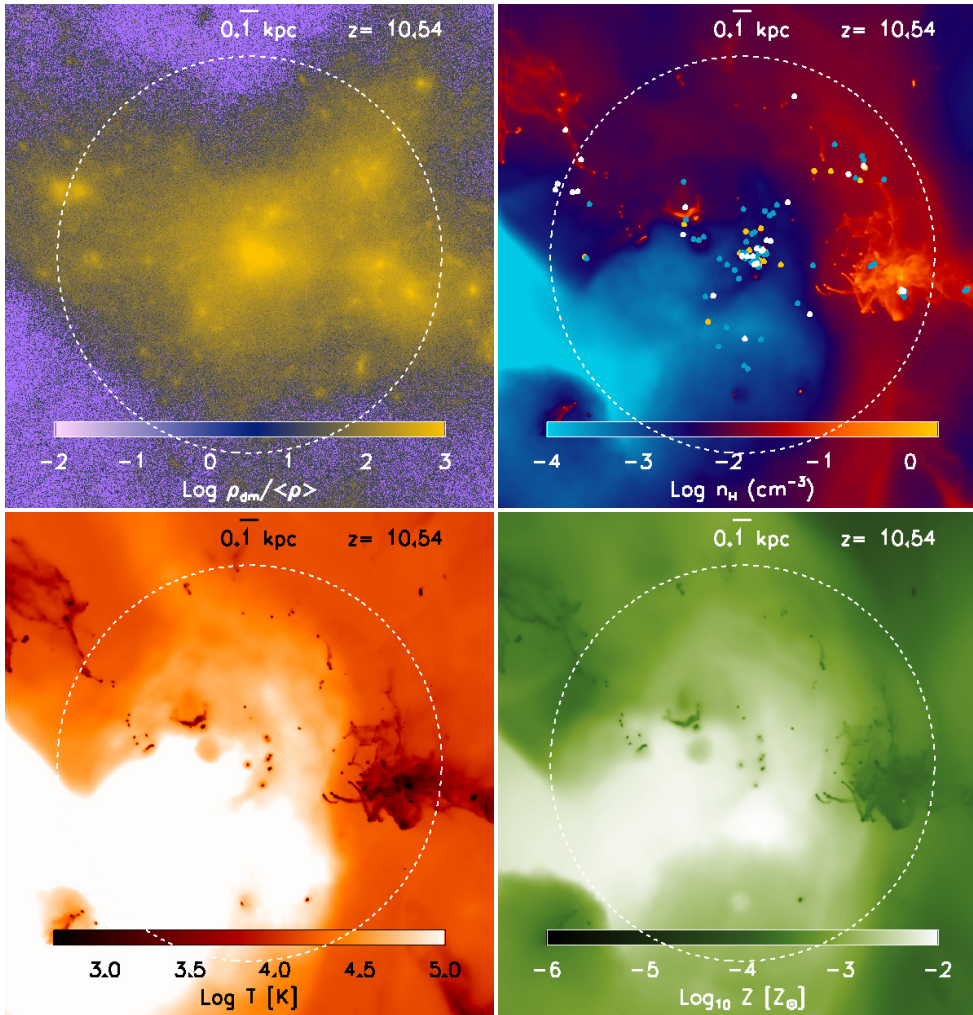


Figure 8. Morphology in the target galaxy at $z \approx 10.5$. *Clockwise from upper left*: Dark matter overdensity, hydrogen number density, gas metallicity, and gas temperature, averaged along the line of sight within the central $\simeq 80$ kpc (comoving). Dashed white circles denote the virial radius, which is $r_{\text{vir}} \approx 1.1$ kpc at this time, with a corresponding virial mass of $M_{\text{vir}} \approx 8 \times 10^7 M_{\odot}$. The positions of the Pop III remnants are marked as filled circles in the upper-right panel: BHs as yellow, neutron stars left behind by lower-mass CCSNe as blue, whereas the location of Pop II clusters are shown in white. Due to the ongoing star formation inside the galaxy, the central gas is substantially evacuated into the void that is roughly perpendicular to the filaments of the cosmic web, resulting in gas densities $n_{\text{H}} \lesssim 10^{-4} \text{ cm}^{-3}$ with temperatures well above 10^6 K due to SN blastwaves. The central region is substantially metal-enriched to $Z \approx 10^{-2} Z_{\odot}$, and all gas inside the virial radius is polluted above $Z = 10^{-5} Z_{\odot}$.

$0.5 M_{\odot} \text{ yr}^{-1}$. At $z = 11.7$, the halo exceeds $3.5 \times 10^7 M_{\odot}$, and fulfills the criterion for the onset of atomic hydrogen cooling (see Fig. 7). At the end of the simulation at $z \approx 10.5$, the target halo has reached a virial mass of $\sim 8 \times 10^7 M_{\odot}$, after undergoing another major merger at $z = 11.3$.

Fig. 7 also shows the growth rates onto the target halo, the evolution of the average gas temperature, and the H I/H II fraction. The gas is photoheated by Pop III and Pop II stars to temperatures of $\sim 10^4$ K, temporarily reaching even higher temperatures in the wake of SN explosions or due to X-ray heating from accreting BHs and HMXBs. Early on, the gas can quickly recombine once an emission source is turned off. However, at $z \approx 12$, about 50% of the gas remains ionized by continuous star formation activity. The morphology of the emerging galaxy at $z \approx 10.5$ is shown in Fig. 8. Along a direction roughly perpendicular to the filaments of the cosmic web, the gas is highly evacuated to $n_{\text{H}} < 10^{-4} \text{ cm}^{-3}$ by Pop II stellar feedback, heating it to $T \sim 10^6 - 10^7$ K and enriching it to $Z \sim 10^{-2.5} Z_{\odot}$ (see the bottom panels of Fig. 7).

3.2.2 Star formation history

Until $z = 12.5$, star formation in the target halo is dominated by Pop III stars, but afterwards Pop II stars form out of metal-enriched gas, and become the dominant stellar population. By the end of the simulation, the emerging target halo has hosted 15 accreting BHs, 2 HMXBs, 40 Pop III CCSNe, possibly leaving neutron stars behind, and 31 Pop II clusters. The total mass of the stellar remnants increases from $\sim 100 M_{\odot}$ at $z \approx 28$ to $3 \times 10^4 M_{\odot}$ at $z \approx 10.5$ (see the left-upper panel of Fig. 7). However, not all of them are formed inside the halo. In order to determine their birth places, we trace their trajectories in Fig. 9, by recording their distances from the center of the target halo. We find that 30% of the remnants, corresponding to 15% in mass, formed in neighboring haloes and were subsequently accreted by the target halo.

One of the key physical quantities of the galaxy is the total stellar mass, needed to predict its observational signature. Given the extremely short lifetime of Pop III stars, of order a few Myr,

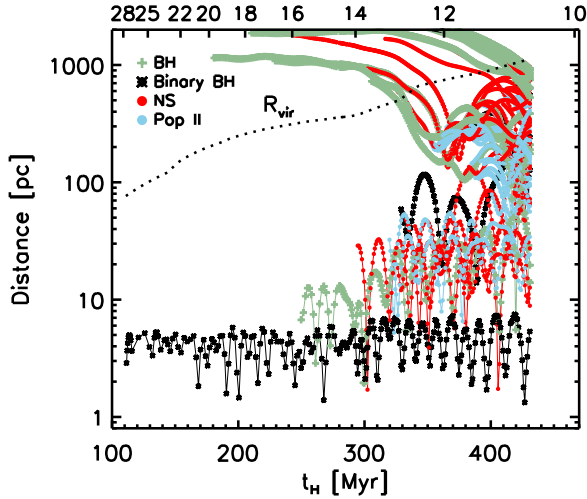


Figure 9. Trajectories of all stellar remnants formed during the assembly process of the target galaxy. The dotted line denotes the virial radius of the halo. As can be seen, about 30% of the remnants, corresponding to 15% of total remnant mass, formed in neighboring haloes and were incorporated into the target halo. The majority of Pop II clusters are born in-situ, out of gas inside the galaxy, and only 3 clusters arise from mergers.

we only consider Pop II clusters to estimate the stellar mass, computed as $M_{*,\text{Pop II}} \propto \int_{m_{\min}}^{m_{\max}} m^{-\alpha} m \, dm$, where the IMF slope is $\alpha = 1.35$, and the lower mass limit $m_{\min} = 0.1 M_{\odot}$. The upper mass limit, m_{\max} , on the other hand, is time variable and depends on the age of the Pop II cluster, such that only stars with a main-sequence lifetime larger than the age of the cluster contribute to the persistent stellar mass. The estimated stellar mass in the halo starts from $540 M_{\odot}$ at $z \approx 13$ and increases to $6 \times 10^3 M_{\odot}$ at $z \approx 10.5$. The corresponding star formation rate (SFR) is a few $\sim 10^{-4} M_{\odot} \text{ yr}^{-1}$.

The small characteristic mass for Pop III stars, $M_{\text{char}} = 20 M_{\odot}$, adopted in this simulation, results in a qualitatively very different star formation and galaxy assembly history, compared with the $M_{\text{char}} = 100 M_{\odot}$, which was often used in previous first galaxy formation work (Bromm & Yoshida 2011). For instance, our simulation employs the same initial conditions as those in Greif et al. (2010) and Jeon et al. (2012), both of which used $M_{\text{char}} = 100 M_{\odot}$ for Pop III stars and neglected the Pop III/Pop II transition. Greif et al. (2010) showed that the strong feedback from a single PISN and its progenitor, formed at the beginning of their simulation at $z \approx 28$, evacuates most of the gas out of the host halo. Except for one additional star at $z \approx 14$, the halo remained without further star formation for the next ~ 300 Myr after the PISN. More stars formed in the simulation of Jeon et al. (2012), where the target halo hosted a total of 8 stars in the presence of the positive X-ray feedback from an accreting BH source. To the contrary, the same target halo here forms a total of 52 Pop III stars and 31 Pop II clusters by the end of the simulation. This striking difference in the star formation history reflects the relative strength of radiative and mechanical feedback from Pop III stars, depending on their masses: photoheating from massive Pop III stars strongly evacuates the gas and suppresses further star formation, as demonstrated in Greif et al. (2010) and Jeon et al. (2012).

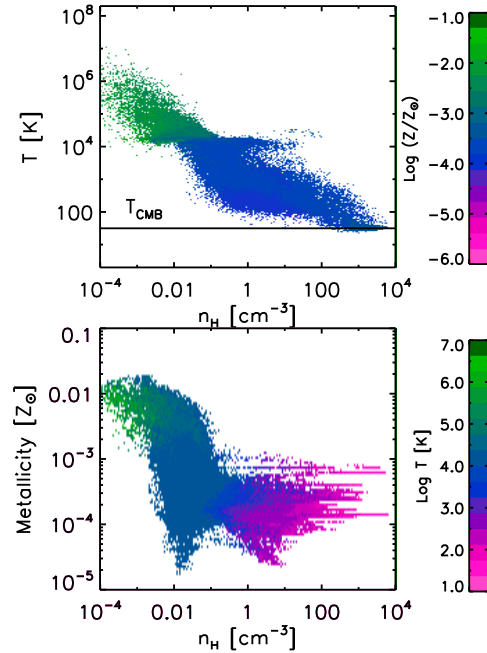


Figure 10. *Top:* Density-temperature phase diagram of the gas inside the target galaxy at $z \approx 10.5$. The color coding indicates gas metallicity. Thanks to the metal cooling, high density gas ($n_{\text{H}} \gtrsim 100 \text{ cm}^{-3}$) is able to cool down to the CMB temperature floor at ~ 30 K. *Bottom:* Density-metallicity phase diagram. The color coding now indicates gas temperature. The metallicity spread in the range $Z = 10^{-4} - 10^{-3} Z_{\odot}$ for high density gas, which is mainly responsible for subsequent star formation, implies that both Pop III and Pop II might form in the enriched gas, but this depends on the choice of critical metallicity (see main text). Note that the gas with $n_{\text{H}} < 0.01 \text{ cm}^{-3}$ is highly enriched to $\sim 0.01 Z_{\odot}$, due to the recent SN explosion in the rarified region established by photoheating from its progenitor.

3.2.3 Metal enrichment

The 40 Pop III and 248 Pop II CCSNe that exploded in the target halo produce a total of $28 M_{\odot}$ and $70 M_{\odot}$ in metals, respectively. Most (60%) of the metals are permanently ejected from the target system into the diffuse IGM, leaving only $40 M_{\odot}$ of metals in the galaxy, supplied partially by the re-accretion of metals, or provided by in-situ SN events. The mass-weighted, average gas metallicity in the galaxy is $\langle Z \rangle = 7 \times 10^{-4} Z_{\odot}$ at $z \approx 10.5$, whereas that of the densest gas, out of which new stars form, is higher by a factor of ~ 30 .

A notable difference from many previous studies is that *all* the heavy chemical elements inside the target galaxy are produced by CCSNe, and not in PISN events. Despite the smaller yield $y = 0.05$ for CCSNe, in contrast to $y = 0.5$ for PISNe, and the smaller masses of $M_{\text{char}} = 20 M_{\odot}$ for Pop III stars, the total mass in metals, now provided by a large number of Pop III CCSNe, is comparable to the metal production by a single $200 M_{\odot}$ PISN. The result is a level of overall metal enrichment similar to previous studies. For instance, the central gas within a $M_{\text{vir}} \approx 10^8 M_{\odot}$ halo at $z \approx 10$ is enriched to an average of $\sim 10^{-3} Z_{\odot}$ by a single $200 M_{\odot}$ PISN (e.g. Greif et al. 2010). With a series of PISN events, the central gas cloud in $M_{\text{vir}} = 5 \times 10^7 - 10^8 M_{\odot}$ haloes could be enriched to

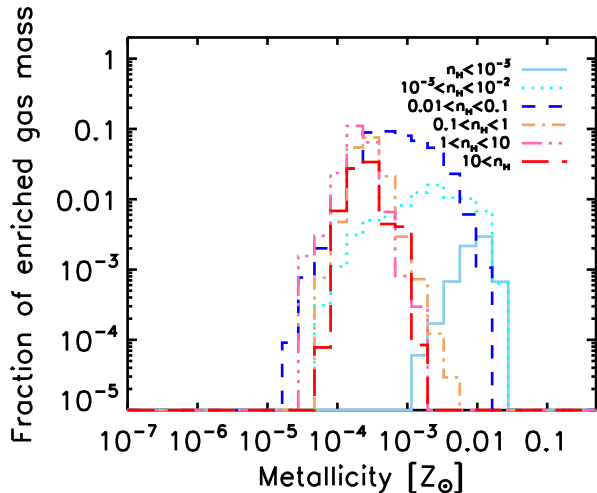


Figure 11. Enriched gas mass fraction within the virial radius of the galaxy as a function of metallicity at $z \approx 10.5$. It can be seen that the peak remains roughly at $Z = 10^{-4} - 10^{-3} Z_{\odot}$ for all densities, except for the lowest density gas, with $n_{\text{H}} < 0.01 \text{ cm}^{-3}$, which shows a peak at $\gtrsim 10^{-3} Z_{\odot}$. This is due to a recent SN explosion, which is preferentially propagating along the underdense region of the galaxy.

$[Z/H] = -2.5 - 3.0$, as well (e.g. Wise et al. 2012; Biffi & Maio 2013). Therefore, we emphasize that while the choice of characteristic Pop III mass results in substantially different star formation histories, as discussed above, the degree of metal enrichment might be similar whether a first galaxy is enriched by a single or a few energetic PISNe, or by numerous CCSNe.

To gain further insight into the stellar population mix in our target galaxy, in Fig. 10 we show the gas temperature (top) and gas metallicities (bottom) inside the galaxy as a function of hydrogen density at $z \approx 10.5$. The metallicities of the high-density gas ($n_{\text{H}} \gtrsim 10^3 \text{ cm}^{-3}$), which is the main reservoir for star formation, are in the range $10^{-4} Z_{\odot}$ to $10^{-3} Z_{\odot}$. As a result, instead of having a clear termination of Pop III star formation, both populations may coexist within the galaxy. Lowering the critical metallicity, however, as suggested by the dust-cooling theories, would lead to exclusively Pop II star formation inside the target system. Gas temperatures reach the floor set by the CMB at $\sim 30 \text{ K}$ (horizontal line in the top panel of Fig. 10), due to efficient metal fine-structure line cooling. Without it, the gas would only be able to cool to $\sim 200 \text{ K}$ via molecular hydrogen cooling. Overall, 40% of the gas mass within the galaxy is enriched above the critical metallicity for fine-structure cooling, and no primordial gas ($Z \lesssim 10^{-5} Z_{\odot}$) remains. As shown in Fig. 11, across all densities, the gas metallicity peaks at $10^{-4} - 10^{-3} Z_{\odot}$, excluding the lowest densities, $n_{\text{H}} \lesssim 0.01 \text{ cm}^{-3}$, where the peak is located above $10^{-3} Z_{\odot}$. This difference is associated with recent metal pollution in low density regions, which are already highly evacuated by photoheating from the massive SN progenitor.

The bright afterglow spectra of possible Pop III gamma-ray bursts (GRBs), with absorption lines imprinted by intervening metal-enriched clouds, would be an ideal tool for probing the metal enrichment of the early Universe simulated here (e.g. Wang et al. 2012; Macpherson et al. 2013). Specifically, the equivalent widths of the metal absorption spectra may allow us to distinguish whether the first heavy elements were produced by a PISN or a CCSN, and

in turn constrain the Pop III IMF (e.g. Wang et al. 2012). As we have discussed in Section 3.1, the diffuse, low column density, IGM may be the preferred hunting ground for a possible PISN enrichment signature, whereas the higher-column density systems may be dominated by the conventional CCSN signature.

3.3 Stellar and galactic archeology

A promising method to constrain the properties of primordial stars is to probe the metal-poor stars in the halo of our Milky Way, or in nearby dwarf satellite galaxies. This approach, often termed stellar or galactic archeology (e.g. Frebel et al. 2010; Brown et al. 2012; Karlsson et al. 2013; Vargas et al. 2013; Milosavljević & Bromm 2014), is based on the assumption that such metal-poor halo stars were born out of gas that was polluted by a single or a few Pop III SNe, and have survived until the present day, thus preserving the signature of the first generation of stars (e.g. Simon et al. 2015). In particular, investigating the metallicity distribution of metal-poor stars, the so-called metallicity distribution function (MDF) (see Beers & Christlieb 2005 for a thorough review), places constraints on several key physical quantities, such as the critical metallicity, Z_{crit} , and the characteristic mass of Pop III stars. The MDF for the metal-poor Milky Way halo stars exhibits a peak at $[\text{Fe}/\text{H}] \approx -2$, and rapidly declines toward lower metallicities with a sharp cutoff at $[\text{Fe}/\text{H}] \approx -4$.

The semi-analytical study by Salvadori et al. (2007), where a Monte Carlo methodology based on an analytic Press-Schechter merger-tree is employed, shows that their model for which $Z_{\text{crit}} = 10^{-4} Z_{\odot}$ and $M_{\text{Pop III, char}} = 200 M_{\odot}$ can nicely reproduce the observed Galactic halo MDF, except for the existence of hyper metal-poor stars below $[\text{Fe}/\text{H}] = -5$. Fig. 12 shows the MDF of Pop II stars in our simulation, within the target halo (red) and within the more extended high-resolution region (black), evaluated at the end of our simulation at $z \approx 10.5$. We should mention that stellar metallicities, Z_{s} , are different from the gas metallicities discussed in previous sections. The stellar metallicity is inherited from the gas metallicity when a star is born out of its birth cloud. For the conversion between Z_{s} and $[\text{Fe}/\text{H}]$, we use the relation $[\text{Fe}/\text{H}] \simeq \log_{10}(Z_{\text{s}}/Z_{\odot}) - 0.25$, adopting the relative iron fraction produced by Pop III stars (Heger & Woosley 2010). The cutoff at $[\text{Fe}/\text{H}] = -3.75$ arises from the critical metallicity $Z_{\text{crit}} = 10^{-3.5} Z_{\odot}$ adopted here, below which Pop II stars cannot form. Thus, all stellar metallicities exceed $[\text{Fe}/\text{H}] = -3.75$ by design, and the maximum is at $[\text{Fe}/\text{H}] = -3.75$ and $[\text{Fe}/\text{H}] = -3.55$ for the target halo and the high-resolution region, respectively.

The stellar metallicity is determined by a complex interplay between the strength of photoheating by Pop III stars and the ability of haloes to retain their gas. In a halo with a shallow potential or in a halo hosting a massive Pop III star, the stellar metallicity of Pop II stars tends toward the metallicity of the reincorporated gas that was ejected out of the host halo by a previous SN blastwave. On the other hand, if photoheating is not strong, as is usually the case for the low mass Pop III stars ($M_{\text{Pop III}} \lesssim 40 M_{\odot}$), or if a host halo is massive, Pop II stars are likely to be born out of the gas that is highly enriched, because after a SN explosion the ejected metals remain in the central region and the central gas density remains high, promptly triggering Pop II star formation.

We should caution that our MDF is not directly comparable to the observed MDF, particularly to the low-metallicity tail of the observed MDF ($[\text{Fe}/\text{H}] < -3.75$). The main reason for the lack of these extremely metal-poor (EMP) stars in the simulated MDF is due to the critical metallicity we adopt. Hence, in order to include

such stars we might use a lower value of the critical metallicity. The other way of explaining EMP stars would be to assume that low mass, long-lived metal-free stars ($M_{\text{Pop III}} < 0.8 M_{\odot}$) were formed, and that their surfaces were polluted externally later on by accretion of gas enriched with metals (e.g. Shigeeyama et al. 2003; Trenti & Shull 2010; Johnson & Khochfar 2011).

One of the interesting open questions in high- z galaxies is whether or not we can find any fossils of the first galaxies in the Local Group, especially in local dwarf galaxies (see Tolstoy et al. 2009 for a review; see also e.g. Bovill & Ricotti 2009; Simpson et al. 2013; Milosavljević & Bromm 2014). One widely discussed scenario for the origin of dwarf galaxies invokes the suppression of their gas supply due to reionization (e.g. Salvadori & Ferrara 2009). Specifically, most stars are argued to have formed before reionization in haloes with $M_{\text{vir}} = 10^8 - 10^9 M_{\odot}$, giving rise to systems that have then passively evolved into a subset of the dwarf galaxies. Next to reionization, photoheating and SN feedback act to evacuate the gas from the haloes. This scenario would naturally explain both the old age of the extant stellar populations, and the absence of any ongoing star formation in dwarf galaxies. However, the probability of a galaxy formed near the reionization era to remain intact and isolated, not undergoing mergers, is small, of order $\approx 10\%$ (Sasaki 1994). Therefore, only a subset of the present-day Local Group dwarfs might be suitable candidates for comparison with the first galaxies (Frebel & Bromm 2012; Frebel et al. 2014).

Fig. 13 shows the relation between the mean metallicity of metal-poor stars and their masses in dwarf galaxies of the Milky Way and M 31 (Kirby et al. 2013). Assuming that stellar metallicities remain unchanged until today, the estimated mean metallicity of our simulated galaxy is $\langle [\text{Fe}/\text{H}] \rangle \approx -3.3$, which is lower by ≈ 0.5 dex than what is expected from the empirical relation, $\langle [\text{Fe}/\text{H}] \rangle \approx -1.69 + 0.30 \log_{10}(M_*/10^6 M_{\odot})$ (see equ. 4 in Kirby et al. 2013). However, our simulation ends before reionization is complete. Indeed, further star formation and metal enrichment will likely occur, leading to Pop II stars with higher metallicities. The effect of this missing activity may be to raise the average metallicity, possibly up to levels consistent with the empirical Kirby-relation. Therefore, tracing the evolution of the galaxy to $z \simeq 5$, and ideally even beyond that, might be necessary to directly compare simulation results with observations.

To infer the star formation history of dwarf galaxies, Webster et al. (2014) have recently performed simulations that follow the evolution of an isolated system with a dark matter mass of $\sim 10^7 M_{\odot}$ for 600 Myr, accounting for metal enrichment by Type II and Type Ia SNe. They found that their simulated system has a mean metallicity of $[\text{Fe}/\text{H}] = -2.1$ and a stellar mass of $2 \times 10^3 M_{\odot}$ after 600 Myr, suggesting Segue 1 as the closest observed match (see also Frebel et al. 2014). However, their simulation is performed in a small region (< 400 pc) with a rather idealized setup. In particular, their high mean metallicity is caused by the assumption of an enrichment floor that is linearly increasing with the number of SNe. On the other hand, Pop II SN enrichment in our simulation does not impose any artificial metallicity floor, thus enabling lower metallicity conditions.

3.4 Luminosity

One of the imminent challenges for the next generation of telescopes, such as the *JWST*, is to detect the first light from high-redshift dwarf galaxies in the early Universe. In order to assess the detectability of these sources, we compute the expected bolometric and line emission luminosities for the simulated galaxy. Due to

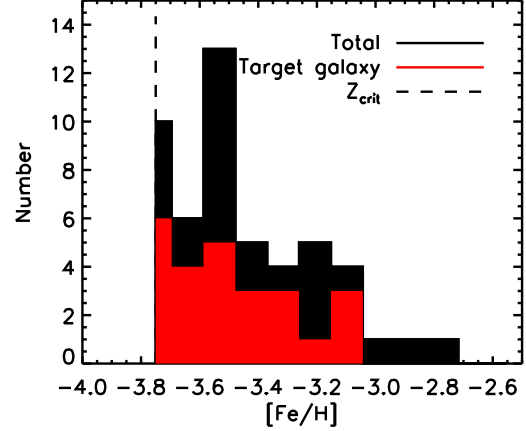


Figure 12. Metallicity distribution function (MDF) of Pop II stars formed by the end of the simulation. The MDF peaks at $Z_s = 10^{-3.5} Z_{\odot}$ and $Z_s = 10^{-3.3} Z_{\odot}$, respectively, for the stars inside the target halo (red) and for all Pop II stars in the high-resolution region (black). The lower cutoff is a consequence of the adopted critical metallicity, which may be lower in reality.

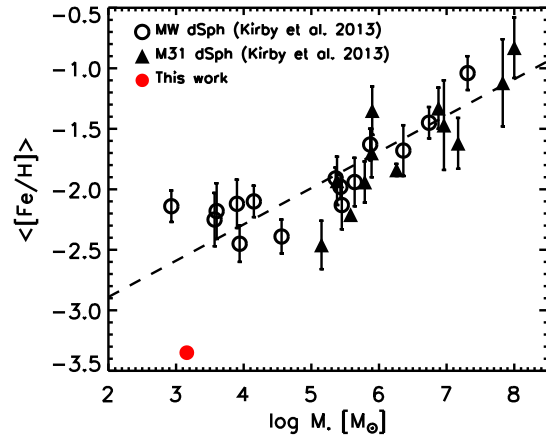


Figure 13. Stellar mass–mean metallicity relation from observations of dwarf galaxies around our Milky Way and M 31. They are strongly correlated, well fitted by the formula $\langle [\text{Fe}/\text{H}] \rangle \approx -1.69 + 0.30 \log_{10}(M_*/10^6 M_{\odot})$, shown as the dashed line (Kirby et al. 2013). For comparison, we also plot the estimate for the mean metallicity of our simulated galaxy (red dot). This value is lower than the empirical relation by ≈ 1 dex, implying that the simulated system cannot give rise to the observed local dwarfs. However, see the main text for further discussion.

the short lifetime of Pop III stars, we only consider emission from Pop II stars. Assuming an instantaneous starburst, the bolometric luminosity from a Pop II cluster is represented by the following equation,

$$L_{\text{Bol, Pop II}} \propto \int_{m_{\text{min}}}^{m_{\text{max}}} m^{-\alpha} \phi(m) dm, \quad (10)$$

where $\phi(m)$ is the mass-luminosity relation. Depending on the mass of a star, a different power-law is used: $L \propto m^{2.3}$ ($m < 0.43 M_{\odot}$), $L \propto m^4$ ($0.43 M_{\odot} < m < 2 M_{\odot}$), $L \propto m^{3.5}$ ($2 M_{\odot} < m < 20 M_{\odot}$), and $L \propto m$ ($m > 20 M_{\odot}$). Additionally,

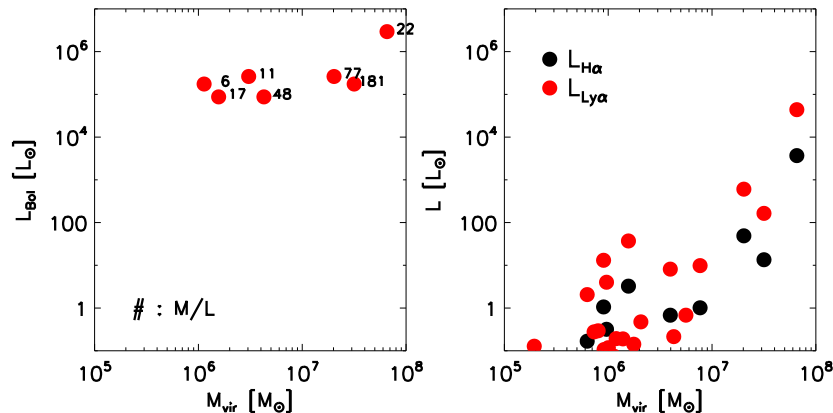


Figure 14. Bolometric luminosity (*left*) and recombination line luminosity from $H\alpha$ and $Ly\alpha$ (*right*) for haloes hosting Pop II clusters. The target galaxy has a bolometric luminosity of $L_{\text{Bol}} = 3.5 \times 10^6 L_{\odot}$. Except for this target galaxy, the bolometric luminosities of the other haloes are of order a few times $10^5 L_{\odot}$. The numbers next to the red dots in the left panel indicate the mass-to-light ratios, which are quite large, similar to that of the local dwarf galaxies. The recombination line luminosities from $H\alpha$ and $Ly\alpha$ are smaller than L_{Bol} by 1 – 4 orders of magnitude.

we compute the nebular emission, i.e. the luminosity in recombination lines, particularly for $H\alpha$ and $Ly\alpha$, from the surrounding gas that is ionized by star formation (e.g. Johnson et al. 2009),

$$L_{H\alpha} = \sum_i j_{H\alpha} \frac{m_i}{\rho_i} \left[\frac{\rho_i}{\mu_i m_H} \right]^2 f_e f_{\text{HII}}, \quad (11)$$

$$L_{Ly\alpha} = \sum_i j_{Ly\alpha} \frac{m_i}{\rho_i} \left[\frac{\rho_i}{\mu_i m_H} \right]^2 f_e f_{\text{HII}}, \quad (12)$$

where j is the temperature-dependent emission coefficient of the lines (Osterbrock & Ferland 2006), and f_e and f_{HII} are the fractions of electrons and H II ions of the SPH particles inside the virial volume of a given halo.

Fig. 14 shows that the most massive halo with a mass $M_{\text{vir}} \sim 8 \times 10^7 M_{\odot}$, hosting the target galaxy, has a bolometric luminosity of $L_{\text{Bol}} = 3.5 \times 10^6 L_{\odot}$. We note that 20% of Pop II clusters (out of 34) are younger than 20 Myr, and these are the main contributors to the luminosity. For the other less massive haloes in the mass range of $M_{\text{vir}} = [1.2 \times 10^6 M_{\odot}, 3 \times 10^7 M_{\odot}]$, the bolometric luminosity varies in the range of $L_{\text{Bol}} = [8.7 \times 10^4 L_{\odot}, 2.6 \times 10^5 L_{\odot}]$. Our estimates are consistent with those in Wise et al. (2014), who use a more sophisticated stellar population model to derive bolometric luminosity. As stated above, we only consider the luminosity from Pop II clusters. We should note, however, that the simulated target galaxy continues to form Pop III stars as well, out of the gas with metallicity below $Z_{\text{crit}} = 10^{-3.5} Z_{\odot}$. At $z \approx 10.5$, the galaxy hosts 6 Pop III stars with a total luminosity of $1.4 \times 10^6 L_{\odot}$, corresponding to 40% of the Pop II bolometric luminosity. Thus, adding the contribution from Pop III stars, the combined luminosity may increase roughly by a factor of ~ 1.4 .

Using our bolometric luminosity estimates, we can predict the observed flux at a rest-frame wavelength of $\lambda_e = 1500\text{\AA}$, characteristic of the soft (non-ionizing) UV continuum. The observed continuum flux for an unresolved object is given by (e.g. Oh 1999; Bromm et al. 2001)

$$f_{\nu}(\lambda_o) = \frac{L_{\nu}(\lambda_e)}{4\pi d_L^2(z)} (1+z) \quad (13)$$

$$\sim 1 \text{ nJy} \left(\frac{L_{\nu}(\lambda_e)}{10^{27} \text{ erg s}^{-1} \text{ Hz}^{-1}} \right) \left(\frac{1+z}{11} \right)^{-1}, \quad (14)$$

where d_L is the luminosity distance to a source at redshift z , which is ~ 100 Gpc at $z = 10$. The predicted flux for the galaxy ($M_{\text{vir}} = 8 \times 10^7 M_{\odot}$) in our simulation is $\approx 10^{-3}$ nJy for $L_{\text{Bol}} = 3.5 \times 10^6 L_{\odot}$. This is smaller by two orders of magnitude than the detection limit of the Near Infrared Camera (NIRCam) on-board the *JWST* for extremely deep imaging (e.g. Gardner 2006). Therefore, more promising targets for detection with the *JWST* will be more massive, luminous, systems with $M_{\text{vir}} = 10^9 - 10^{10} M_{\odot}$ (e.g. Pawlik & Schaye 2011). The other possible way of detecting those small galaxies is through gravitational lensing with a boost in brightness by a factor of $\mu \sim 100$ (e.g. Zackrisson et al. 2012, 2015). However, magnifications of $\mu > 100$ are extremely rare, mainly due to the low probability of having sight lines for the gravitational lensing, $P(> \mu) \propto \mu^{-2}$ (e.g. Pei 1993), requiring very large survey areas to find the lensed galaxies.

On the other hand, the nebular emission in recombination lines are $L_{H\alpha} = 4 \times 10^3 L_{\odot}$ and $L_{Ly\alpha} = 4.8 \times 10^4 L_{\odot}$, respectively, both of which are even weaker than the bolometric luminosity by 2 – 3 orders of magnitude. This is mainly due to the low gas densities as a result of the photoheating from the newly forming stars, resulting in low recombination rates. In our estimate, we have assumed escape fractions for $H\alpha$ and $Ly\alpha$ photons of unity, rendering the calculated line luminosities upper limits. Although the recombination luminosity in $Ly\alpha$ is higher than that in $H\alpha$, in reality $Ly\alpha$ photons are more likely to scatter in the neutral IGM (e.g. Dijkstra & Wyithe 2007; Smith et al. 2015), and thus the observed flux in $Ly\alpha$ may be substantially lower than implied by the intrinsic luminosity. Because of the hard spectra of massive Pop III stars, strong nebular emission, particularly in the He II $\lambda 1640$ line, has been suggested as a possible observable signature of metal-free Pop III galaxies (e.g. Schaerer 2003; Dawson et al. 2004; Nagao et al. 2008; Johnson et al. 2009; Cai et al. 2015). However, as implied by our simulation, the gas inside the first galaxies is likely already metal-enriched, and thus their stellar content is expected to be dominated by Pop II, instead of Pop III, stars, making it more

difficult to use the recombination lines as a probe to detect such metal-enriched small systems.

Finally, a complementary method is to look for counterparts of the first galaxies in the Local Group. Assuming, probably unrealistically so, that star formation in our simulated galaxy is completely quenched after $z \approx 10.5$, and that it has passively evolved until the present day, the total stellar mass is $1.4 \times 10^3 M_\odot$ at $z = 0$ for the IMF we use. This is comparable to the stellar mass $M_* = 900 M_\odot$ of Segue 2, the least luminous dwarf galaxy known in the local Universe (Kirby et al. 2013). More high-resolution observations of the faintest galaxies are needed to further elucidate the connection between the fossils of the first galaxies and local dwarf galaxies.

4 SUMMARY AND DISCUSSION

We have carried out a radiation hydrodynamical simulation of a galaxy reaching a mass of $M_{\text{vir}} = 8 \times 10^7 M_\odot$ at $z \approx 10$. This simulation tracked ionizing photons from individual Pop III stars and from Pop II clusters. High spatial resolution allowed us to explicitly account for the mechanical and chemical feedback from CCSNe and PISNe. Additionally, we followed the transport of X-ray photons from accreting black holes (BHs) and high mass X-ray binaries (HMXBs). Motivated by recent works on primordial star formation, which suggest Pop III stars with a few tens of M_\odot , we adopted a characteristic mass, $M_{\text{char}} = 20 M_\odot$ for the Pop III IMF. This is substantially smaller than $M_{\text{char}} = 100 M_\odot$, which has been used in most previous studies. We also investigated the metal enrichment history in the early Universe, including the transition in star formation mode from metal-free Pop III stars to low-mass, metal-enriched Pop II stars at the critical metallicity $Z_{\text{crit}} = 10^{-3.5} Z_\odot$. Our main results are as follows.

(i) Adopting a moderate characteristic mass $M_{\text{char}} = 20 M_\odot$, instead of $M_{\text{char}} = 100 M_\odot$, for the Pop III IMF, results in a substantially different star formation history during the assembly process of the target halo that hosts the first galaxy. This is caused by the relatively weak stellar feedback, particularly photoheating, from the less massive Pop III stars.

(ii) The gas inside the galaxy is enriched to $Z_{\text{avg}} \sim 10^{-3} Z_\odot$ by a total of 40 Pop III and 248 Pop II core-collapse supernovae (CCSNs). Despite the striking difference in the star formation history, the degree of metal enrichment by CCSNe is comparable to that by a single $200 M_\odot$ Pop III pair-instability supernova (PISN).

(iii) The metals produced by two PISNe outside the main galaxy are mainly responsible for the metal enrichment in the diffuse IGM, setting a metallicity floor of $Z = 10^{-4} Z_\odot$. Therefore, signatures of PISNe in the early Universe may be found by studying the state of the IGM, e.g. employing bright Pop III GRB afterglows.

(iv) There is no gas with metallicity $Z \lesssim 10^{-5} Z_\odot$ inside the main galaxy. Given the critical metallicity $Z_{\text{crit}} = 10^{-3.5} M_\odot$ adopted here, Pop III stars continue to form out of the gas in the metallicity range $10^{-5} Z_\odot \lesssim Z \lesssim 10^{-3.5} Z_\odot$. Thus, both Pop III and Pop II stars coexist. This conclusion, however, is uncertain, as the critical metallicity may well be lower, which would not allow any extended Pop III star formation.

(v) Due to the rarity of HMXBs and their short life-

times, in combination with the low BH accretion rates $\dot{M}_{\text{BH}} = 10^{-9} - 10^{-12} M_\odot \text{yr}^{-1}$, the impact of X-rays on the gas inside haloes that host X-ray sources and on the IGM is negligible in this simulation.

(vi) The bolometric luminosity of the simulated galaxy is $L_{\text{Bol}} \approx 3.5 \times 10^6 L_\odot$ and the total stellar mass is $6 \times 10^3 M_\odot$ at $z \approx 10.5$. Therefore, the UV flux of the galaxy, redshifted into the near-IR is $1.4 \times 10^{-3} \text{ nJy}$, significantly less than the detection limit for NIRCcam onboard the *JWST*.

(vii) The estimated metal distribution function (MDF) of Pop II stars in the galaxy peaks at $[\text{Fe}/\text{H}] = -3.75$ and the stellar metallicities are in the range $[\text{Fe}/\text{H}] = [-3.75, -2.7]$ with a mean metallicity of $[\text{Fe}/\text{H}] = -3.3$. The stellar mass of $M_* = 1.4 \times 10^3 M_\odot$ of the simulated galaxy, passively evolved to the present day, is comparable to that of Segue 2, the least luminous dwarf known in the local Universe.

It has often been pointed out that including a physically motivated description of stellar feedback is crucial for modeling galaxy formation, especially for small galaxies, which are susceptible to stellar feedback due to their shallow potential wells (e.g. Wise et al. 2012; Kim et al. 2013; Hopkins et al. 2014). We confirm that stellar feedback plays a crucial role in shaping the properties of the first galaxies: by reducing the baryon fraction ($f_{\text{bar}} \approx 0.05$), corresponding to 15% of the cosmic mean, and by enriching the gas to an average of $\langle Z \rangle \approx 10^{-3} Z_\odot$, making Pop II star formation the dominant mode inside the first galaxies. However, galaxies may continue to form Pop III stars because not all gas is enriched above the critical metallicity.

In our simulation, we needed to fix a large number of numerical input parameters, such as the random sampling of the Pop III stellar masses from the underlying IMF. Given that computational resources limit us to only one such realization from a very large ensemble of likely parameter choices, the question arises what aspects of our simulation are contingent on the specific choice, and which results are likely robust. An example of a robust feature is that the first galaxies were already metal-enriched, such that their stellar content is expected to be Pop II; the precise level of this ‘bedrock metallicity’, on the other hand, is uncertain, but likely of order $Z_{\text{avg}} > 10^{-4} Z_\odot$ at $z \approx 10$. An example of a contingent, numerical-parameter dependent feature is the impact of X-ray feedback from early HMXB sources. We mention that X-ray feedback is negligible in our simulation, but the population of HMXBs, which are likely the strongest X-ray sources, and their luminosity and duty-cycle are unknown at high redshifts. We refer the reader to Jeon et al. (2012) for discussion of a case where X-ray feedback is more significant.

We show that the stellar mass fraction in halos is $f_* = M_*/M_{\text{vir}} \sim 10^{-4}$, which is smaller by an order of magnitude than the values found in other studies, for example Behroozi et al. (2013) and O’Shea et al. (2015), using abundance-matching techniques and grid-based simulations, respectively. However, the scatter from their work is large, such that f_* ranges from 10^{-5} to 10^{-1} at a given mass of $M_{\text{vir}} = 10^8 M_\odot$. On the other hand, our estimated for f_* is in a good agreement with the results from Garrison-Kimmel et al. (2014), in which they use an updated abundance-matching technique and reproduce the stellar mass functions of the Milky Way and Andromeda satellites more accurately. The fact that near the end of our simulation the baryon fraction of the target halo is significantly reduced to 15% of the cosmic mean, leading to a

reduction in star formation, robustly implies a highly feedback-regulated regime. Such inefficiency of star formation could be attributed to how we implement stellar feedback, especially the efficiency of SN feedback. However, even if the stellar mass were increased by a factor of 10 by adopting a different parameter implementation, this system would still be observationally out of reach for the *JWST*, at least in the absence of gravitational lensing.

Whether fine-structure line cooling or dust-continuum cooling was mainly responsible for Pop II star formation is still debated (e.g. Omukai 2000; Bromm et al. 2001; Schneider et al. 2002; Bromm & Loeb 2003b; Omukai et al. 2005; Schneider & Omukai 2010; Schneider et al. 2012; Chiaki et al. 2014; Ji et al. 2014). If we had adopted a critical metallicity $Z_{\text{crit,dust}} = 10^{-5.5} Z_{\odot}$, set by dust continuum cooling, the assembly history of the target galaxy would have proceeded quite differently. Adopting a lower critical metallicity than $Z_{\text{crit}} = 10^{-3.5} Z_{\odot}$ would boost the relative importance of Pop II star formation, and long-lived Pop II stars could hence contribute to the total stellar mass. The estimated MDF of Pop II stars would also be changed depending on the critical metallicity. The nature and observational properties of the first galaxies thus sensitively depend not only on the mass scale of the first stars, as has previously been pointed out (Bromm & Yoshida 2011), but also on additional astrophysical parameters, such as the critical metallicity.

Considerable uncertainties remain in the treatment of metal mixing. We used a subgrid model (Greif et al. 2009) in which we assume that the efficiency of metal mixing below the resolved scales is determined by physical quantities at resolved scales. Shen et al. (2010) propose a new implementation to more accurately capture the turbulent mixing in SPH. Further theoretical and observational studies are required to better understand the metal mixing process. As discussed, exploring a large range of parameters is needed to derive representative characteristics of high- z dwarf galaxies. However, performing such a comprehensive suit of high-resolution, radiation-hydrodynamical simulations is computationally challenging.

As mentioned above, the direct detection of the simulated galaxy, with $M_{\text{vir}} \lesssim 10^8 M_{\odot}$, will be out of reach even for the *JWST*, unless extreme, and probably unattainable, gravitational lensing magnifications are involved. Therefore, a more promising strategy to infer their nature may be to use “stellar” or “galactic” archeology by searching for metal-poor stars in the Milky Way or in nearby dwarf galaxies. To fully unleash its potential, both simulations and observational surveys need to be pushed further, a process that clearly has been set in motion now.

ACKNOWLEDGEMENTS

We are grateful to Volker Springel, Joop Schaye, and Claudio Dalla Vecchia for letting us use their versions of GADGET and their data visualization and analysis tools. We thank Jun-Hwan Choi for discussions on the simulation results. V. B. and M. M. acknowledge support from NSF grants AST-1009928 and AST-1413501. A. H. P. receives funding from the European Union’s Seventh Framework Programme (FP7/2007-2013) under grant agreement number 301096-proFeSsoR. We acknowledge access to compute resource Supermuc based in Germany at LRZ Garching provided by the Gauss Centre for Supercomputing/Leibniz Supercomputing Centre under grant:pr83le and by PRACE (proposal number 2013091919). The authors acknowledge the Texas Advanced Computing Center at The University of Texas at Austin for providing HPC resources under XSEDE allocation TG-AST120024

REFERENCES

- Abel T., Bryan G. L., Norman M. L., 2002, *Science*, 295, 93
 Alvarez M. A., Bromm V., Shapiro P. R., 2006, *ApJ*, 639, 621
 Alvarez M. A., Wise J. H., Abel T., 2009, *ApJ*, 701, L133
 Barkana R., Loeb A., 2007, *Rep. Prog. Phys.*, 70, 627
 Bate M. R., Burkert A., 1997, *MNRAS*, 288, 1060
 Beers T. C., Christlieb N., 2005, *ARA&A*, 43, 531
 Behroozi P. S., Wechsler R. H., Conroy C., 2013, *ApJ*, 770, 57
 Belczynski K., Bulik T., Fryer C. L., 2012, (arXiv:1208.2422)
 Biffi V., Maio U., 2013, *MNRAS*, 436, 1621
 Bondi H., Hoyle F., 1944, *MNRAS*, 104, 273
 Bouwens R. J., Illingworth G. D., Oesch P. A., Labbé I., Trenti M., van Dokkum P., Franx M., Stiavelli M., Carollo C. M., Magee D., Gonzalez V., 2011, *ApJ*, 737, 90
 Bovill M. S., Ricotti M., 2009, *ApJ*, 693, 1859
 Bromm V., 2013, *Rep. Prog. Phys.*, 76, 112901
 Bromm V., Coppi P. S., Larson R. B., 2002, *ApJ*, 564, 23
 Bromm V., Ferrara A., Coppi P. S., Larson R. B., 2001, *MNRAS*, 328, 969
 Bromm V., Kudritzki R. P., Loeb A., 2001, *ApJ*, 552, 464
 Bromm V., Loeb A., 2003a, *ApJ*, 596, 34
 Bromm V., Loeb A., 2003b, *Nature*, 425, 812
 Bromm V., Yoshida N., 2011, *ARA&A*, 49, 373
 Brown T. M., Tumlinson J., Geha M., Kirby E. N., VandenBerg D. A., Muñoz R. R., Kalirai J. S., Simon J. D., Avila R. J., Guhathakurta P., Renzini A., Ferguson H. C., 2012, *ApJL*, 753, L21
 Cai Z., Fan X., Jiang L., Davé R., Oh S. P., Yang Y., Zabludoff A., 2015, *ApJL*, 799, L19
 Chabrier G., 2003, *Publ. Astron. Soc. Pac.*, 115, 763
 Chatzopoulos E., Wheeler J. C., 2012, *ApJ*, 748, 42
 Chiaki G., Schneider R., Nozawa T., Omukai K., Limongi M., Yoshida N., Chieffi A., 2014, *MNRAS*, 439, 3121
 Chiaki G., Yoshida N., Kitayama T., 2013, *ApJ*, 762, 50
 Ciardi B., Ferrara A., 2005, *Space Sci. Rev.*, 116, 625
 Clark P. C., Glover S. C. O., Klessen R. S., Bromm V., 2011, *ApJ*, 727, 110
 Dawson S., Rhoads J. E., Malhotra S., Stern D., Dey A., Spinrad H., Januzzi B. T., Wang J., Landes E., 2004, *ApJ*, 617, 707
 Dijkstra M., Wyithe J. S. B., 2007, *MNRAS*, 379, 1589
 Dopcke G., Glover S. C. O., Clark P. C., Klessen R. S., 2013, *ApJ*, 766, 103
 Durier F., Dalla Vecchia C., 2012, *MNRAS*, 419, 465
 Finkelstein S. L. e. a., 2013, *Nature*, 502, 524
 Frebel A., Bromm V., 2012, *ApJ*, 759, 115
 Frebel A., Simon J. D., Geha M., Willman B., 2010, *ApJ*, 708, 560
 Frebel A., Simon J. D., Kirby E. N., 2014, *ApJ*, 786, 74
 Fryer C. L., Heger A., 2000, *ApJ*, 541, 1033
 Furlanetto S. R., Oh S. P., Briggs F. H., 2006, *Physics Reports*, 433, 181
 Gardner J. P. e. a., 2006, *Space Sci. Rev.*, 123, 485
 Garrison-Kimmel S., Boylan-Kolchin M., Bullock J. S., Kirby E. N., 2014, *MNRAS*, 444, 222
 Glover S. C. O., Brand P. W. J. L., 2003, *MNRAS*, 340, 210
 Glover S. C. O., Jappsen A.-K., 2007, *ApJ*, 666, 1
 Gnedin N. Y., 2000, *ApJ*, 542, 535
 Greif T. H., Bromm V., Clark P. C., Glover S. C. O., Smith R. J., Klessen R. S., Yoshida N., Springel V., 2012, *MNRAS*, 424, 399
 Greif T. H., Glover S. C. O., Bromm V., Klessen R. S., 2010, *ApJ*, 716, 510
 Greif T. H., Johnson J. L., Bromm V., Klessen R. S., 2007, *ApJ*, 670, 1
 Greif T. H., Johnson J. L., Klessen R. S., Bromm V., 2008, *MNRAS*, 387, 1021
 Greif T. H., Johnson J. L., Klessen R. S., Bromm V., 2009, *MNRAS*, 399, 639
 Greif T. H., Springel V., White S. D. M., Glover S. C. O., Clark P. C., Smith R. J., Klessen R. S., Bromm V., 2011, *ApJ*, 737, 75
 Haardt F., Madau P., 2012, *ApJ*, 746, 125
 Haiman Z., Thoul A. A., Loeb A., 1996, *ApJ*, 464, 523

- Heger A., Fryer C. L., Woosley S. E., Langer N., Hartmann D. H., 2003, *ApJ*, 591, 288
- Heger A., Woosley S. E., 2002, *ApJ*, 567, 532
- Heger A., Woosley S. E., 2010, *ApJ*, 724, 341
- Hernquist L., Springel V., 2003, *MNRAS*, 341, 1253
- Hirano S., Hosokawa T., Yoshida N., Umeda H., Omukai K., Chiaki G., Yorke H. W., 2014, *ApJ*, 781, 60
- Hopkins P. F., Kereš D., Oñorbe J., Faucher-Giguère C.-A., Quataert E., Murray N., Bullock J. S., 2014, *MNRAS*, 445, 581
- Hosokawa T., Omukai K., Yoshida N., Yorke H. W., 2011, *Science*, 334, 1250
- Hummel J. A., Stacy A., Jeon M., Oliveri A., Bromm V., 2014, (arXiv:1407.1847)
- Inoue A. K., 2011, *MNRAS*, 415, 2920
- Jeon M., Pawlik A. H., Bromm V., Milosavljević M., 2014a, *MNRAS*, 440, 3778
- Jeon M., Pawlik A. H., Bromm V., Milosavljević M., 2014b, *MNRAS*, 444, 3288
- Jeon M., Pawlik A. H., Greif T. H., Glover S. C. O., Bromm V., Milosavljević M., Klessen R. S., 2012, *ApJ*, 754, 34
- Ji A. P., Frebel A., Bromm V., 2014, *ApJ*, 782, 95
- Johnson J. L., Bromm V., 2006, *MNRAS*, 366, 247
- Johnson J. L., Dalla Vecchia C., Khochfar S., 2013, *MNRAS*, 428, 1857
- Johnson J. L., Greif T. H., Bromm V., Klessen R. S., Ippolito J., 2009, *MNRAS*, 399, 37
- Johnson J. L., Khochfar S., 2011, *MNRAS*, 413, 1184
- Karlsson T., Bromm V., Bland-Hawthorn J., 2013, *Rev. Mod. Phys.*, 85, 809
- Kim J.-h., Krumholz M. R., Wise J. H., Turk M. J., Goldbaum N. J., Abel T., 2013, *ApJ*, 779, 8
- Kirby E. N., Boylan-Kolchin M., Cohen J. G., Geha M., Bullock J. S., Kaplinghat M., 2013, *ApJ*, 770, 16
- Kirby E. N., Cohen J. G., Guhathakurta P., Cheng L., Bullock J. S., Galazzi A., 2013, *ApJ*, 779, 102
- Kitayama T., Yoshida N., 2005, *ApJ*, 630, 675
- Kitayama T., Yoshida N., Susa H., Umemura M., 2004, *ApJ*, 613, 631
- Klessen R. S., Lin D. N., 2003, *Physical Review E*, 67, 046311
- Krumholz M. R., McKee C. F., Klein R. I., 2005, *ApJ*, 618, 757
- Kuhlen M., Madau P., 2005, *MNRAS*, 363, 1069
- Loeb A., Furlanetto S. R., 2013, *The First Galaxies in the Universe* (Princeton University Press, Princeton, NJ)
- Macpherson D., Coward D. M., Zadnik M. G., 2013, *ApJ*, 779, 73
- Maio U., Ciardi B., Dolag K., Tornatore L., Khochfar S., 2010, *MNRAS*, 407, 1003
- Maio U., Khochfar S., Johnson J. L., Ciardi B., 2011, *MNRAS*, 414, 1145
- McKee C. F., Ostriker E. C., 2007, *ARA&A*, 45, 565
- Milosavljević M., Bromm V., 2014, *MNRAS*, 440, 50
- Milosavljević M., Bromm V., Couch S. M., Oh S. P., 2009a, *ApJ*, 698, 766
- Milosavljević M., Couch S. M., Bromm V., 2009b, *ApJ*, 696, L146
- Mirabel I. F., Dijkstra M., Laurent P., Loeb A., Pritchard J. R., 2011, *A&A*, 528, A149
- Mitsuda K., Inoue H., Koyama K., Makishima K., Matsuoka M., Ogawara Y., Suzuki K., Tanaka Y., Shibasaki N., Hirano T., 1984, *PASJ*, 36, 741
- Muratov A. L., Gnedin O. Y., Gnedin N. Y., Zemp M., 2013, *ApJ*, 773, 19
- Nagao T., Sasaki S. S., Maiolino R., Grady C., Kashikawa N., Ly C., Malkan M. A., Motohara K., Murayama T., Schaerer D., Shioya Y., Taniguchi Y., 2008, *ApJ*, 680, 100
- Nomoto K., Tominaga N., Umeda H., Kobayashi C., Maeda K., 2006, *Nuclear Physics A*, 777, 424
- Oesch P. A., Bouwens R. J., Illingworth G. D., Gonzalez V., Trenti M., van Dokkum P. G., Franx M., Labbé I., Carollo C. M., Magee D., 2012, *ApJ*, 759, 135
- Oh S. P., 1999, *ApJ*, 527, 16
- Oh S. P., Haiman Z., 2002, *ApJ*, 569, 558
- Okamoto T., Gao L., Theuns T., 2008, *MNRAS*, 390, 920
- Omukai K., 2000, *ApJ*, 534, 809
- Omukai K., Tsuribe T., Schneider R., Ferrara A., 2005, *ApJ*, 626, 627
- O’Shea B. W., Wise J. H., Xu H., Norman M. L., 2015, (arXiv:1503.01110)
- Osterbrock D. E., Ferland G. J., 2006, *Astrophysics of gaseous nebulae and active galactic nuclei* (CA: University Science Books)
- Park K., Ricotti M., 2012, *ApJ*, 747, 9
- Pawlik A. H., Milosavljević M., Bromm V., 2011, *ApJ*, 731, 54
- Pawlik A. H., Milosavljević M., Bromm V., 2013, *ApJ*, 767, 59
- Pawlik A. H., Schaye J., 2008, *MNRAS*, 389, 651
- Pawlik A. H., Schaye J., 2011, *MNRAS*, 412, 1943
- Pawlik A. H., Schaye J., van Scherpenzeel E., 2009, *MNRAS*, 394, 1812
- Pei Y. C., 1993, *ApJ*, 403, 7
- Power C., Wynn G. A., Combet C., Wilkinson M. I., 2009, *MNRAS*, 395, 1146
- Prieto J., Padoan P., Jimenez R., Infante L., 2011, *ApJ*, 731, L38
- Pringle J. E., 1981, *ARA&A*, 19, 137
- Ricotti M., Gnedin N. Y., Shull J. M., 2002, *ApJ*, 575, 49
- Ritter J. S., Safrank-Shrader C., Gnat O., Milosavljević M., Bromm V., 2012, *ApJ*, 761, 56
- Ritter J. S., Sluder A., Safrank-Shrader C., Milosavljević M., Bromm V., 2014, (arXiv:1408.0319)
- Robertson B. E., Ellis R. S., Dunlop J. S., McLure R. J., Stark D. P., 2010, *Nature*, 468, 49
- Robertson B. E., Furlanetto S. R., Schneider E., Charlot S., Ellis R. S., Stark D. P., McLure R. J., Dunlop J. S., Koekemoer A., Schenker M. A., Ouchi M., Ono Y., Curtis-Lake E., Rogers A. B., Bowler R. A. A., Cirasuolo M., 2013, *ApJ*, 768, 71
- Safrank-Shrader C., Agarwal M., Federrath C., Dubey A., Milosavljević M., Bromm V., 2012, *MNRAS*, 426, 1159
- Safrank-Shrader C., Milosavljević M., Bromm V., 2014b, *MNRAS*, 440, L76
- Saitoh T. R., Makino J., 2009, *ApJ*, 697, L99
- Salvadori S., Ferrara A., 2009, *MNRAS*, 395, L6
- Salvadori S., Schneider R., Ferrara A., 2007, *MNRAS*, 381, 647
- Sasaki S., 1994, *PASJ*, 46, 427
- Scannapieco E., Schneider R., Ferrara A., 2003, *ApJ*, 589, 35
- Schaerer D., 2002, *A&A*, 382, 28
- Schaerer D., 2003, *A&A*, 397, 527
- Schaye J., Dalla Vecchia C., Booth C. M., Wiersma R. P. C., Theuns T., Haas M. R., Bertone S., Duffy A. R., McCarthy I. G., van de Voort F., 2010, *MNRAS*, 402, 1536
- Schenker M. A., Ellis R. S., Konidaris N. P., Stark D. P., 2014, *ApJ*, 795, 20
- Schmidt W., Federrath C., 2011, *A&A*, 528, A106
- Schneider R., Ferrara A., Natarajan P., Omukai K., 2002, *ApJ*, 571, 30
- Schneider R., Omukai K., 2010, *MNRAS*, 402, 429
- Schneider R., Omukai K., Limongi M., Ferrara A., Salvaterra R., Chieffi A., Bianchi S., 2012, *MNRAS*, 423, L60
- Shen S., Wadsley J., Stinson G., 2010, *MNRAS*, 407, 1581
- Shigeyama T., Tsujimoto T., Yoshii Y., 2003, *ApJL*, 586, L57
- Shull J. M., Harness A., Trenti M., Smith B. D., 2012, *ApJ*, 747, 100
- Simon J. D., Jacobson H. R., Frebel A., Thompson I. B., Adams J. J., Sheckman S. A., 2015, *ApJ*, 802, 93
- Simpson C. M., Bryan G. L., Johnston K. V., Smith B. D., Mac Low M.-M., Sharma S., Tumlinson J., 2013, *MNRAS*, 432, 1989
- Smith A., Safrank-Shrader C., Bromm V., Milosavljević M., 2015, *MNRAS*, 449, 4336
- Smith R. J., Glover S. C. O., Clark P. C., Greif T., Klessen R. S., 2011, *MNRAS*, 414, 3633
- Springel V., 2005, *MNRAS*, 364, 1105
- Springel V., White S. D. M., Tormen G., Kauffmann G., 2001, *MNRAS*, 328, 726
- Stacy A., Bromm V., Loeb A., 2011, *MNRAS*, 413, 543
- Stacy A., Greif T. H., Bromm V., 2010, *MNRAS*, 403, 45
- Stacy A., Greif T. H., Bromm V., 2012, *MNRAS*, 422, 290
- Stark D. P., Richard J., Charlot S., Clément B., Ellis R., Siana B., Robertson B., Schenker M., Gutkin J., Wofford A., 2015, *MNRAS*, 450, 1846
- Stinson G. S., Brook C., Macciò A. V., Wadsley J., Quinn T. R., Couchman H. M. P., 2013, *MNRAS*, 428, 129

- Susa H., Hasegawa K., Tominaga N., 2014, *ApJ*, 792, 32
- Tegmark M., Silk J., Rees M. J., Blanchard A., Abel T., Palla F., 1997, *ApJ*, 474, 1
- Tolstoy E., Hill V., Tosi M., 2009, *ARA&A*, 47, 371
- Trenti M., Shull J. M., 2010, *ApJ*, 712, 435
- Trenti M., Stiavelli M., Michael Shull J., 2009, *ApJ*, 700, 1672
- Turk M. J., Abel T., O'Shea B., 2009, *Science*, 325, 601
- Umeda H., Nomoto K., 2005, *ApJ*, 619, 427
- Vargas L. C., Geha M., Kirby E. N., Simon J. D., 2013, *ApJ*, 767, 134
- Wang F. Y., Bromm V., Greif T. H., Stacy A., Dai Z. G., Loeb A., Cheng K. S., 2012, *ApJ*, 760, 27
- Webster D., Sutherland R., Bland-Hawthorn J., 2014, *ApJ*, 796, 11
- Whalen D., Abel T., Norman M. L., 2004, *ApJ*, 610, 14
- Whalen D., van Veelen B., O'Shea B. W., Norman M. L., 2008, *ApJ*, 682, 49
- Wheeler J. C., Johnson V., 2011, *ApJ*, 738, 163
- Wiersma R. P. C., Schaye J., Theuns T., Dalla Vecchia C., Tornatore L., 2009, *MNRAS*, 399, 574
- Wiklund T., Mobasher B., Bromm V., eds, 2013, *The First Galaxies* Vol. 396 of *Astrophysics and Space Science Library*
- Wise J. H., Abel T., 2007, *ApJ*, 665, 899
- Wise J. H., Abel T., 2008, *ApJ*, 685, 40
- Wise J. H., Demchenko V. G., Halicek M. T., Norman M. L., Turk M. J., Abel T., Smith B. D., 2014, *MNRAS*, 442, 2560
- Wise J. H., Turk M. J., Norman M. L., Abel T., 2012, *ApJ*, 745, 50
- Wolcott-Green J., Haiman Z., Bryan G. L., 2011, *MNRAS*, 418, 838
- Xu H., Ahn K., Wise J. H., Norman M. L., O'Shea B. W., 2014, *ApJ*, 791, 110
- Xu H., Wise J. H., Norman M. L., 2013, *ApJ*, 773, 83
- Yoon S.-C., Dierks A., Langer N., 2012, *A&A*, 542, A113
- Yoshida N., Abel T., Hernquist L., Sugiyama N., 2003, *ApJ*, 592, 645
- Yoshida N., Oh S. P., Kitayama T., Hernquist L., 2007, *ApJ*, 663, 687
- Yoshida N., Omukai K., Hernquist L., Abel T., 2006, *ApJ*, 652, 6
- Zackrisson E., González J., Eriksson S., Asadi S., Safranek-Shrader C., Trenti M., Inoue A. K., 2015, *MNRAS*, 449, 3057
- Zackrisson E., Rydberg C.-E., Schaerer D., Östlin G., Tuli M., 2011, *ApJ*, 740, 13
- Zackrisson E., Zitrin A., Trenti M., Rydberg C.-E., Guaita L., Schaerer D., Broadhurst T., Östlin G., Ström T., 2012, *MNRAS*, 427, 2212